Smart protection of surfaces during day-night by a novel composite self-cleaning coating with catalytic memory

Maryam Mokhtarifar [1,2], Duc Trung Nguyen [1], Mohan Sakar [3], Andrea Lucotti [2], Marco Asa [4], Reyhaneh Kaveh [5], Maria Vittoria Diamanti [2*], MariaPia Pedeferri [2], and Trong-On Do [1*]

[1] *Chemical Engineering Department, Laval University, Quebec City, Canada*

[2] *Department of Chemistry, Materials and Chemical Engineering "G. Natta," Politecnico di Milano, Milan, Italy*

[3] *Centre for Nano and Material Sciences, Jain University, Karnataka, India*

[4] *Department of Physics, Politecnico di Milano, Milan, Italy*

[5] *Department of Chemistry, Sharif University of Technology, Tehran, Iran*

* Corresponding authors: mariavittoria.diamanti@polimi.it , trong-on.do@gch.ulaval.ca

Address for correspondence: Maria Vittoria Diamanti, Department of Chemistry, Materials and Chemical Engineering "G. Natta," Politecnico di Milano, via Mancinelli 7, 20131 Milan, Italy

Abstract: For the first time this work reports a new idea to develop a round-the-clock self-cleaning coating which was successfully applied to preserve cultural heritage and modern artifacts under sunlight illumination and at night. To fabricate this structure, namely, $H_2:TiO_2/WO_3@Pt$, soft templating and hydrogen treatment approaches were selected to enhance the performance of TiO_2/WO_3 photocatalyst, together with the addition of Pt plasmonic nanoparticles. The coating can be photochemically charged in the presence of sacrificial electron donors and keep its stability, benefiting from the remained electrons stock for over 10 hours to clean the surface from aggressive pollution also at night, in absence of light. This transparent heterostructure with high surface area, proper interfacial contacts in $TiO_2/WO_3@$ Pt system, and extended visible light absorption resulting from the synergistic interactions of the composite system (TiO_2, WO_3, and Pt) presents an efficient self-cleaning performance. The smart coated surface could clean the substrate benefiting from 70 % pollutants photodegradation after irradiation followed by dark storage (2 and 6 h, individually), and superhydrophilic properties were maintained for hours in the dark, thanks to oxygen vacancies resulted from hydrogen treatment.

Keywords: Self-cleaning; photocatalysis; TiO_2/WO_3 composite; hydrogen treatment; catalytic memory

1. Introduction: The construction of "Guggenheim museum" in Bilbao, as the first use of modern architecture metal sheathing, started a universal phenomenon named "Bilbao effect"; since then, the use of new metals such as titanium, aluminium, and stainless in the field of modern façades has spread to several other cities. These modern metals show improved corrosion/discoloration resistance, color uniformity, and attractive appearance [1]. However, irrespective of the metal type and the high level of their resistance against corrosion, long-term exposure of the metals to harsh environmental conditions finally reveals its deteriorating effects [2–4]. **Figure 1** shows images of "il Podium Hadid" (2017) and "Guggenheim museum" (1997), located in Milan (Italy) and Bilbao (Spain), made by aluminum and titanium, respectively. As it can be seen, original color (light gray) has changed to different colors from dark gray to blue during just few years. Acid rain and the deposition of aggressive natural/artificial pollution are the main reasons for this deterioration, causing the growth of a metal oxide layer on the surface [5,6]. Since such growth is limited only to the outmost surface layer, removal of the undesirable layer can restore the surfaces to a pre-discolored condition. Yet, it is very challenging to control the exact degree for removal of such a thin oxide layer through chemical or mechanical polishing [1,7,8]. Hence, preventing substrates from discoloration is desirable, considering that cleaning of these huge buildings is so expensive and time consuming. As a matter of fact, using transparent smart coating materials (like TiO_2-based photocatalysts) with self-cleaning properties for further and more effective preservation of the metals have gained a considerable attention [9–12]. However, the biggest limitation of all the common photocatalytic coatings is that they can preserve artifacts only when irradiated, while metallic structures undergo deterioration also in absence of any source of irradiation, for instance at nights. In order to extend their capabilities to the full day-night period, some studies have focused on making their activity independent of photons, upgrading it not only under light irradiation, but also in the dark.

The round-the-clock photocatalysts (RPC) including a composition of a semiconductor (like TiO_2) and a chargeable material (like WO_3), have high potential in practical applications and therefore a unique and more effective RPC system could support the developments in this field [13]. However, the minimal TiO_2/WO_3 heterostructure interface limits charge separation and electron storage abilities. Moreover, photocatalytic activity of the TiO_2/WO_3 in visible region and consequent in dark are both restricted [14–17]. Hence, to protect the artifacts more efficiently, TiO_2/WO_3 based RPCs that absorb both UV and visible light and present a proper charge storage capacity must be

developed. Nowadays, surface modified RPCs prepared by different approaches (e.g. templating and defect engineering) have attracted considerable attention, because they improve photoactivity by enhancing photoabsorption through defects acting as photoinduced charge traps, and increasing the accessibility of active sites for reactants as well as enhancing electron storage abilities; all these features result in improved performances of the RPCs [18–25]. Moreover, the use of plasmonic nanoparticle cocatalysts (like Ni, Ag, and Pt nanoparticles), providing an electron separation pathway to accept stored electrons from WO_3, could be considered to improve TiO_2 photoactivity performance [26–29].

Herein, for the first time, we explore a smart round-the-clock coating combination between a new nanostructured RPC and an efficient de-polluting surface to demonstrate the feasibility for solar energy harvesting, energy storage and self-cleaning capacity of metallic artifacts in one module. This durable RPC coating, namely H_2:TiO_2/WO_3@Pt, can be used to enhance redox reactions between the photoactive surface and contaminants accompanied by energy storage/release.
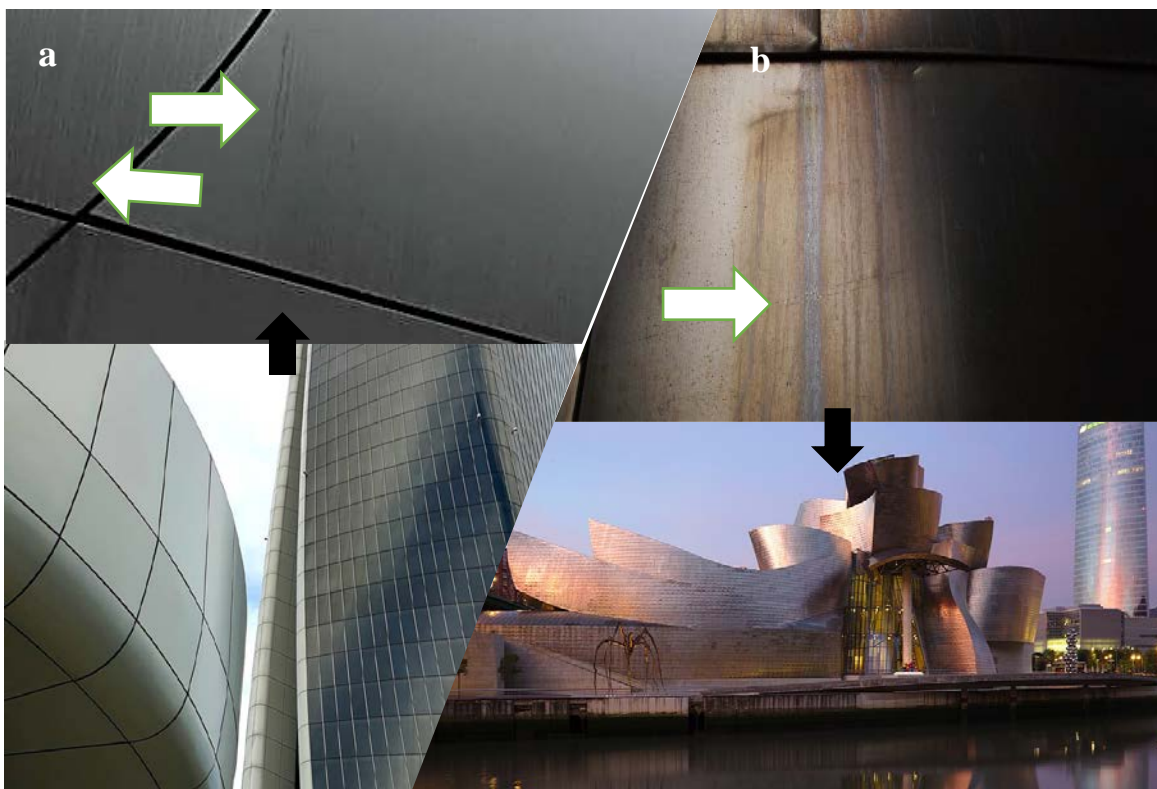
Figure 1. The discoloration in modern metallic artifacts, a) City Life Shopping District (il Podium Hadid), Milan, Italy made by aluminium, b) Guggenheim museum made by titanium, Bibao, Spain (https://commons.wikimedia.org/wiki/File:Bilbao_-_Guggenheim_aurore.jpg).

2. Experimental

2.1. **Materials:** Titanium isopropoxide (TTIP), hexachloride tungstate (WCl_6), D -(+)-Glucose, hydrogen peroxide (H_2O_2), ethanol (EtOH), chloroplatinic acid (H_2PtCl_6), and sodium hexametaphosphate (SHMP) were purchased from Aldrich. All the reagents were used without further purification. Commercial purity titanium sheets (grade 2 ASTM), 0.5 mm thick, were used as substrates for coating deposition.

2.2. **Synthesis of TiO_2/WO_3:** First, three stock solutions were prepared as below. A known amount of D-(+)-Glucose (as the sacrificial template) was dispersed in distilled water (150 mL) by a mixer for 15 min (solution I). 1 g titanium isopropoxide (TTIP) was mixed with H_2O_2 (7 g) and distilled water (43 g), stirred for 15 min (solution II). Solution III was prepared by dissolving an appropriate amount of WCl_6 in 50 mL absolute EtOH, the gradual color change of this solution from yellow to dark blue indicated the solvolysis took place. For the synthesis of

TiO$_2$/WO$_3$, the three solutions were mixed with a stirrer(4 h) , dried at 80 ^{o}C. The obtained solid was calcined at 550 °C for 5 h to remove the template. The prepared sample with TiO$_2$:WO$_3$ ratio of 80:20 was labelled TiO$_2$/WO$_3$.

2.3. *Synthesis of TiO$_2$/WO$_3$@Pt:* The materials were synthesized by the photodeposition method. In a typical procedure, 100 mg TiO$_2$/WO$_3$ nanoparticles were dissolved in methanol (200 ml) , and H$_2$PtCl$_6$ (0.5, 1.5, and 3 wt% aqueous solution) was added. The reaction mixture was illuminated by a sunlight-simulating 150 W Xe lamp (AM 1.5 G, 100 mW cm^2) for 6 h. The resulting TiO$_2$/WO$_3$@Pt composites were washed several times to remove excess methanol, and then dried.

2.4. *Synthesis of H$_2$:TiO$_2$/WO$_3$ and H$_2$:TiO$_2$/WO$_3$@Pt:* The calcined TiO$_2$/WO$_3$ and TiO$_2$/WO$_3$@Pt powders (100 mg each) were treated separately in a hydrogen atmosphere (95% in Argon, flow rate: 200 mL.min^{-1}) at 400 °C for 4 h to obtain H$_2$-treated TiO$_2$/WO$_3$ and TiO$_2$/WO$_3$@Pt particles denoted as H$_2$:TiO$_2$/WO$_3$ and H$_2$:TiO$_2$/WO$_3$@Pt, respectively (**Figure S1**). The ratio of each component of these composite catalysts was optimized on powder samples in the degradation of MeOH (Table S1).

2.5. *Preparation of coatings:* To prepare suspensions of the powders, a 0.005 wt% solution of each sample in de-ionized water (20 mL) was prepared at ambient temperature. Then, the mixtures were dispersed by an ultrasonic bath for 30 min followed by adding SHMP stabilizer (5 wt%) and stirring for 24 h. Then, the titanium substrates (50 x 50 mm ^{2}) were coated with the final sols by dip-coating method [30–37]. The dipping number was fixed to five, and the immersion and withdrawal rates were modulated at 200 and 100 mm/min, respectively. After each dipping, the coated specimens (active surface area: 1.7 x 1.9 cm^2) were dried at 25 ^{o}C for 24 h and final layers were calcinated at 600 ^{o}C for 2 h. The thickness of the film deposited on the specimen coated with H$_2$:TiO$_2$/ WO$_3$@Pt RPC was determined to be about 350 nm (see **Figure S2**).

3. *Characterization:* To study structure, optical properties and photoactivity efficiency, the prepared samples were analyzed using FESEM), XRD, XPS, UV–visible spectroscopy, BET specific surface area analysis, AFM, and electrochemical measurements.

3.1. Structural characterization: In specific, to evaluate BET active surface, the samples were outgassed for 8 h (T: 150 °C) and then the measurements were done using a Quantachrome Autosorb-1 MP analyzer . XRD patterns were obtained with Cu K$_{\alpha 1}$ radiation in a 2θ: 20-60° range using a Philips PW1830 powder diffractometer (scanning rate: 2.5^o/min). UV-visible

absorption was measured in wavelength range of 300–1000 nm using a 300 Bio UV-Vis spectrophotometer. . XPS was done by a photoelectron spectrometer (Kratos Axis Ultra) using X-ray light source (Al Kα; hν = 1486.6 eV). The morphologies of samples were evaluated by field emission scanning electron microscopy (FESEM, TESCANMIRA II). The stability the coated films and crack propagation on their structure was evaluated by optical microscopy (OM) (Leica INM 200). Moreover, adhesion evaluation of the films was done by a microhardness device (FISCHERSCOPE® HM2000) and by comparing OM images of scratched lines produced on the substrates by helping a diamond tip. To study roughness, AFM analysis (NT-MDT AFM Solver Pro) was done on 60 x 60 μm^2 surface area; the coatings were applied on mirror polished titanium specimens.

3.2. Photoelectrochemical characterization: To prepare working electrode, the photocatalyst (20 mg of each sample) was dissolved in distilled water (5 mL) and drop-casted onto a FTO glass (A: 2 cm^2) . Then, the coated glass was dried at 80 ^{o}C for 24 h. The photoelectrochemical measurements were done in 1 M NaOH solution by a system including the coated glasses as working electrode, a platinum wire as counter electrode, and SCE as reference electrode. The EIS and Mott- Schottky measurements were carried out in a frequency 0.1 MHz- 0.1 Hz and 1 kHz, respectively.. The time-profiled OCP tests were performed with a potentiostat (EG&G 263A2) in light off/on under a simulated solar light (150 W Xe lamp).

3.3. Self-cleaning evaluation

3.3.1. Photocatalytic performance: To evaluate photocatalytic performances, samples (1.7 x 1.9 cm^2) were characterized by methylene blue degradation (MB, 40 mL (10^{-5} M)) at the wavelength 668 nm (UV–Vis spectrophotometer, Thermo scientific Spectronic 200E). First, the samples were kept in dark for 50 min in the MB solution reaching adsorption-desorption equilibrium, and then illuminated with UV LED (wavelength: 330-400 nm) and visible LED (wavelength: 400-750 nm) for 6 h. A pseudo-first-order kinetics was hypothesized to control the rate of MB photodegradation, as observed in related scientific literature [38,39], so the slope of the curve of *ln(C/C$_o$)* versus time of reaction was considered rate constant (*k*), being C and C$_o$ the MB concentrations during the test and at time 0.

3.3.2. Wettability: The contact angle of the substrates was studied by measuring the contact angles of water drops (WCA) (5 μl volume) by a CCD camera. These measurements were done

on five different spots on the surfaces before and after 30 min activation by simulated solar light illumination.

3.3.3. Simulated acid rain and artificial soiling tests: To mimic different polluted atmospheres from light to heavy, individual soiling components were prepared and applied to the surface of coated samples by dipping with 45 º immersion angle, to achieve maximum soiling effect with uniform distribution (see **Table 1S**) [40]. **Figure 2** presents different countries with contemporary modern metals-based artifacts and their related pollution states, as examples of locations where pollution could damage metallic artifacts similarly to the artificial environments adopted.

To evaluate the self-cleaning ability of titanium coated with $H_2:TiO_2/WO_3@Pt$ RPC, solar light photoactivated specimens (for 1 h) were dipped in the soiling components immediately and then left to dry. For the study of discoloration resistance through simulating acid rain, uncoated and coated samples were kept in a solution of adjusted pH 4 at 65 °C [40][41]. Then, color changes made by the accelerated soiling and acid rain tests were measured by colorimetry analysis (Konica Minolta 2500d spectrophotometer in reflectance mode) before and after the tests: $\Delta E = \sqrt{(\Delta L^*)^2 + (\Delta a^*)^2 + (\Delta b^*)^2}$.

La Cité du Vin , Sweden

https://www.wallpaperflare.com/building-architecture-planetarium-office-building-dome-wallpaper-ecwkb

Umicore hoboken" by conix architects, Belgium

https://www.flickr.com/photos/agcglasseurope/8435897420

Marques de Riscal Hotel, Spain

https://www.flickr.com/photos/larou/16412215784

Museum of History of Polish Jews, Poland

https://www.flickr.com/photos/polandmfa/8654814768/in/photostream/

MiCo – Milano Convention Center, Italy

https://www.flickr.com/photos/o_0/49470720031/in/photostream/

Good   Light   Moderate   Heavy

Soiling components	Polluted states			
	Good	Light	Moderate	Heavy
Carbon black	8 %	5 %	6 %	12 %
Organics	0 %	8 %	15 %	36 %
Dust	61 %	63 %	52 %	28 %
Inorganics salt	31 %	24 %	27 %	24 %

Figure 2. Varying artificial polluted states and contemporary modern metals-based artifacts located in these states .

4. Results and discussion

4.1. RPC coatings configuration and structure

XRD results are shown in **Figure 3a**, indicating the presence of TiO_2 and WO_3 in the materials. In comparison with TiO_2, where only anatase was detected, the TiO_2/WO_3 structures formed with a mixed anatase/rutile phase. No peak related to Pt was detected, which may be a result of the small size belonging to the Pt nanoparticles. XRD patterns of TiO_2/WO_3 composites are indexed following the standard diffraction patterns of crystalline TiO_2 (JCPDS file No. 21-1272) (JCPDS file No. 21-1276) and WO_3 (JCPDS file No. 75-2187), indicating the high crystallinity of TiO_2/WO_3 heterostructures. The diffraction peaks at 25.5 °, and 27.4 ° correspond to (101) and

(110) crystal planes of anatase and rutile TiO_2, respectively [42][43]. Anatase and rutile contents are estimated from the respective integrated XRD peak intensity by the following equation: $\chi = (1 + 0.8\ I_A/I_R)^{-1}$ [44,45]. While the addition of Pt alone had no effect on crystal structure, probably due to low impurity level, results show a slight increase in rutile content upon hydrogen treatment (**Table 1**). This could be due to reduction conditions of hydrogen thermal environment and also effect of WO_3 incorporation [46–51]. Moreover, the WO_3 crystalline structures are largely affected by hydrogen treatment. The WO_3 crystalline phase is converted to the tetragonal phase at 550 °C with recognized peaks at about 22.6 °, 23.8 °, and 28.3 ° indexed as (002), (110), and (102) planes, respectively [52–57]. The WO_3 phase transition upon hydrogen treatment could be ascribed to the introduction of defects, especially oxygen vacancies, which are beneficial in enhancing the photocatalytic activity and electrochemical performance of WO_3 [54].

UV-Vis spectra of the synthesized samples are displayed in **Figure 3b**. The typical absorption band edge of TiO_2 in H_2:TiO_2/WO_3@Pt is extended to the visible light region, which agrees with the colour change from white to dark gray after H_2 treatment and Pt photodeposition (**Figure S2**). These observed changes in the optical absorption profile of H_2:TiO_2/WO_3@Pt could be attributed to several factors, such as the composite induced electron transitions in the system, oxygen vacancies, and the synergistic optical enhancements due to the integration of multiple systems such as TiO_2, WO_3, and Pt along with the effect of reduction by H_2. Pt nanoparticles could have a notable effect on the reduction of WO_3 in H_2 treatment, as Pt nanoparticles could dissociate chemisorbed H_2 molecules to active hydrogen atoms, which subsequently migrate to the WO_3 particles causing their partial reduction [21] [58].

The morphology of synthesized composites was captured by FESEM images. **Figure 4** shows spherical TiO_2/WO_3 nanoparticles with an average particle size of 400 nm. After H_2 treatment, the TiO_2/ WO_3 composite has a slightly smaller diameter with a higher degree of aggregation, as compared with other samples: this was ascribed to the sintering effect of H_2 treatment [59,60]. As it can be seen in **Figure 5**, the H_2:TiO_2/WO_3@Pt coated substrate presents a uniform structure. The EDS spectrum of the H_2:TiO_2/WO_3@Pt composite indicates the presence of Ti, W, O, and Pt in the selected area. In addition, the elemental mappings of H_2:TiO_2/WO_3@Pt reveal the homogeneous distribution of these elements.

The surface oxidation states of Ti and W in H_2:TiO_2/WO_3@Pt were characterized by XPS (**Figure 6**). The high-resolution XPS spectrum of Ti 2p in H_2:TiO_2/WO_3@Pt shows two characteristic peaks of Ti^{4+} at 458.4 eV and 464.1 eV, inferring no changes in the oxidation states of Ti 2p after H_2 treatment [61,62]. In contrast, three main XPS peaks at 38.4, 36.3 eV, and 41.3 eV were attributed to W^{6+} and W^{5+}, implying that the oxygen vacancies were introduced into WO_3 after H_2 treatment. Apart from these peaks, a change of shape for the W 4f peak, with a broadening of the W $4f_{7/2}$ and W $4f_{5/2}$ peaks, is observed in H_2:TiO_2/WO_3@Pt RPC due to the H_2 treatment, again indicating presence of oxygen vacancies. The oxygen vacancies are beneficial for the performance of WO_3 as they can store electrons by acting as trapping sites. Moreover, the introduction of these defects could enhance the visible-light absorption of H_2:TiO_2/WO_3@Pt sample, which is in agreement with UV-Vis results [63,64].

The specific surface area (S_{BET}) of the H_2:TiO_2/WO_3@Pt confirm an improvement comparing with other samples presented in **Table 1**. This enhancement could be due to the synergistic effect of glucose-derived porosity characteristics and H_2 treatment, providing a higher number of active sites on the surface [65–67].
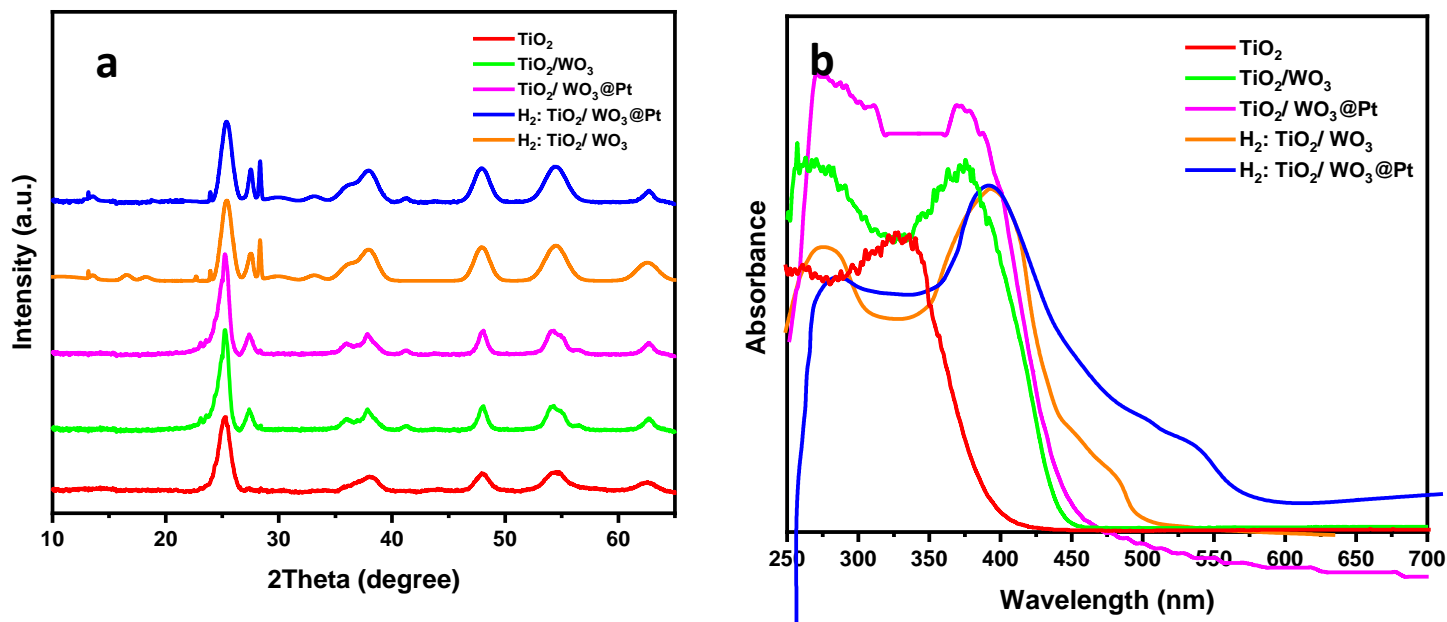
Figure 3. a) XRD patterns and b) UV-vis diffuse reflectance spectra of the TiO_2, TiO_2/WO_3, TiO_2/WO_3@Pt, H_2:TiO_2/WO_3, and H_2:TiO_2/WO_3@Pt thin film.
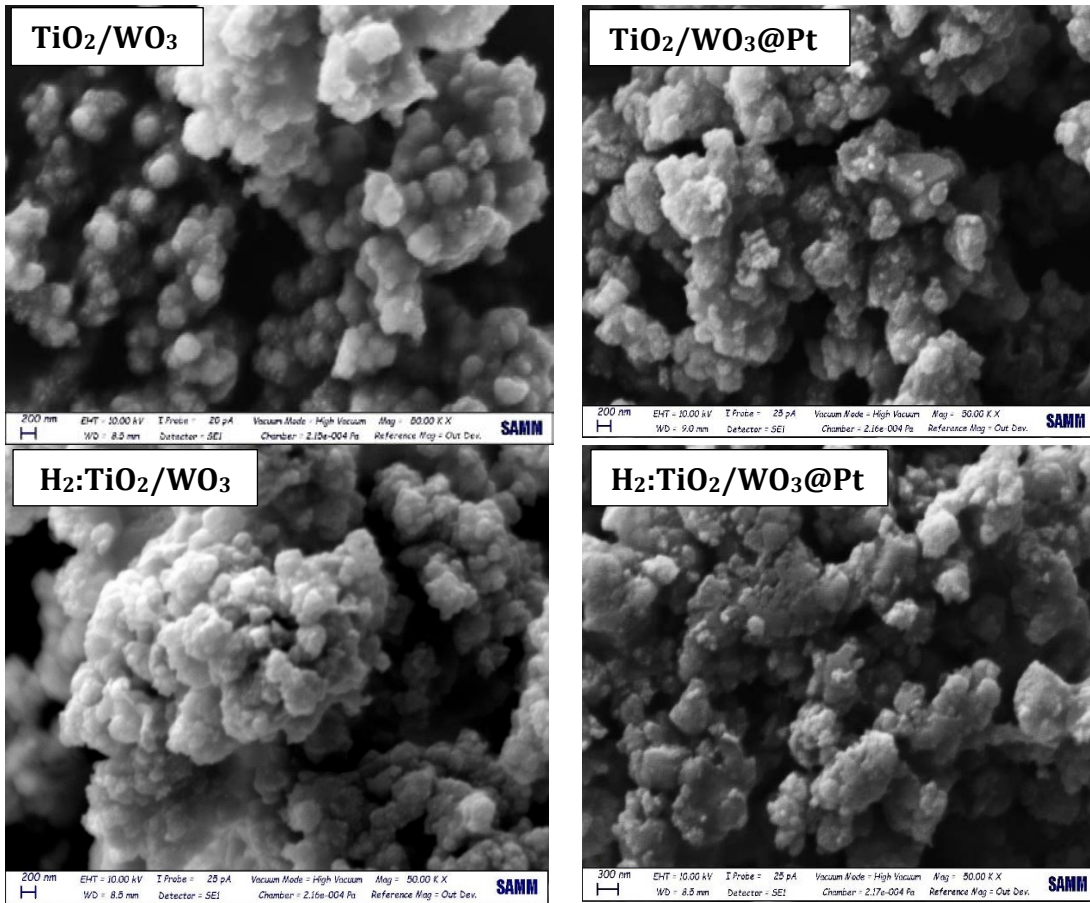
Figure 4. SEM images of structure of the TiO_2/WO_3, $TiO_2/WO_3@Pt$, $H_2: TiO_2/WO_3$, and $H_2: TiO_2/WO_3@Pt$ coatings.
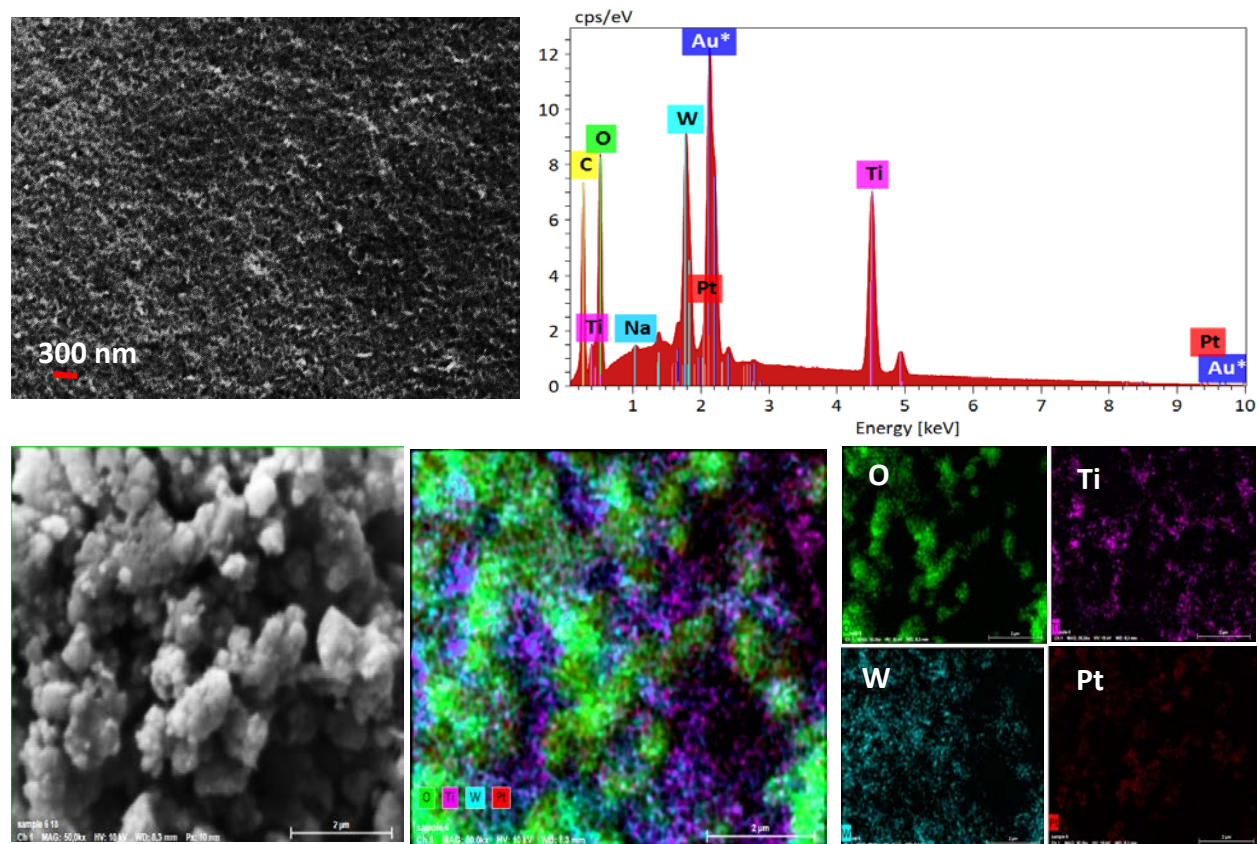
Figure 5. Structure, SEM-EDS spectrum, and EDS mapping results for the H$_2$: TiO$_2$/ WO$_3$@Pt thin film.
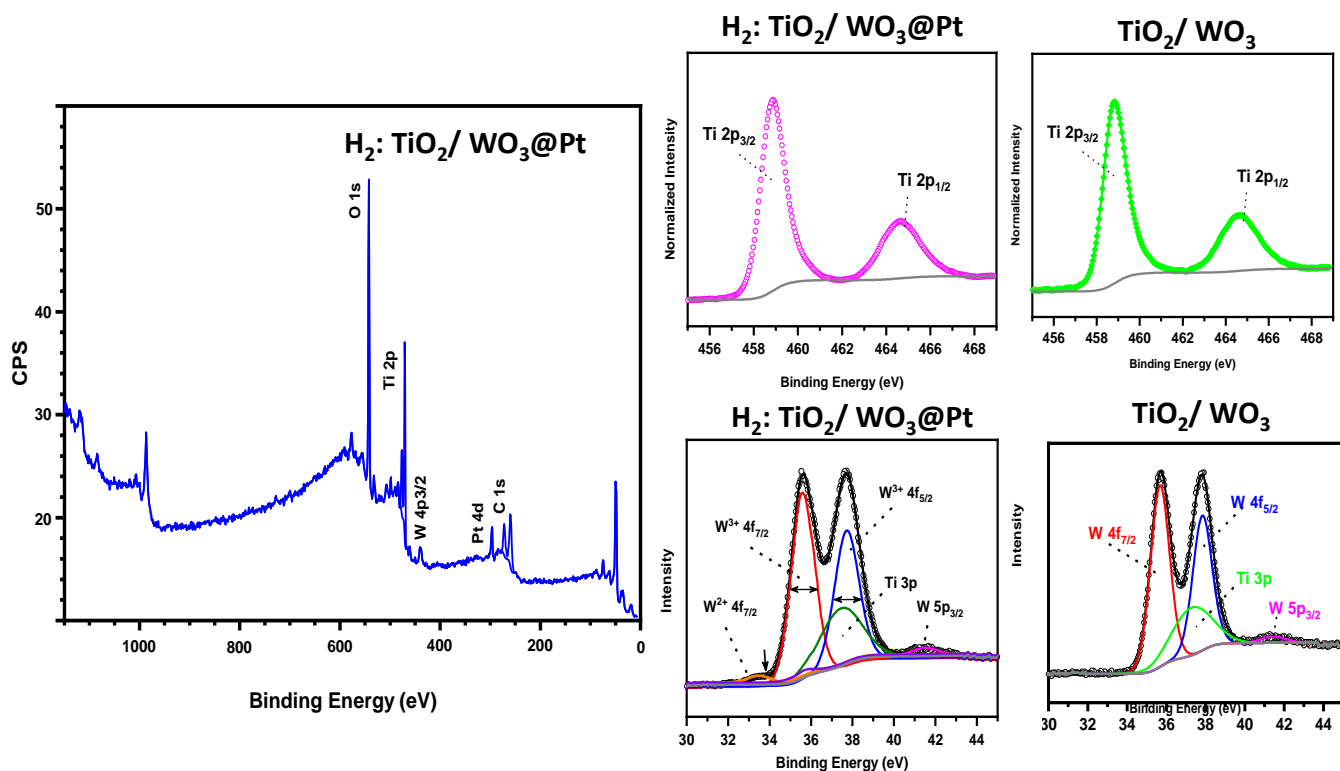
Figure 6. XPS survey and narrow scan spectra (Ti 2p and W 4f) of TiO$_2$/WO$_3$ and H$_2$:TiO$_2$/WO$_3$@Pt RPCs.

The evaluation of transparency and possible color difference between original and protected surface by the RPC coatings is a vital feature to keep the aesthetic appearance of the artifacts [40]. To evaluate this aspect, glass slides were coated with the same procedure of titanium and then transmittance variations were measured. The transmittance results confirmed that all coatings have a satisfactory transmittance, higher than 75% over the whole wavelengths range (**Table 2**). The lower optical transmission of the H$_2$:TiO$_2$/WO$_3$@Pt RPC could be attributed to higher surface roughness and higher absorption intensity in the visible range, as also reported in **Table 2** (see also **Figure S3**). Furthermore, ΔE values in **Table 2** suggest that there is no perceivable color changing between bare and coated glasses. In detail, while the TiO$_2$ coating shows a minimum ΔE (<1), introducing additional components or making hydrogen treatment process only slightly affects ΔE, still below 2.5. The color changing means that these coatings had no meaningful adverse outcome on the aesthetic appearance.

From the aforementioned, an excellent adhesion and mechanical stability of coated films could preserve long-term exposure of the artifacts. Vickers microhardness in different points on the

coatings and related mean values are shown in **Figure 7** and **Table 2**, respectively. It can be confirmed that all samples have a uniform structure, as values measured in different points are similar. Based on the results, the presence of WO3 in the coatings increases hardness values with respect to TiO_2 [68,69]. Surprisingly, the $H_2:TiO_2/WO_3@Pt$ coating presents the highest hardness, as a result of the synergistic effect of WO_3, Pt, and higher rutile content. Rutile crystals play in fact a key role in the hardness of coated films, which is correlated to the stronger adherence to the substrate rather than the anatase phase [70]. Furthermore, the presence of cracks can significantly decrease hardness in comparison to a crack-free films, as discussed in the following.

The surface structure and durability of the coated films were also evaluated by OM images (**Table 3A,B**). In contrast with TiO_2 and WO_3 films, which show cracks on their surface, the other films are crack-free, dense with uniform structures (**Table 3A**). Moreover, the scratch images (**Table 3B**) reveal that the TiO_2/WO_3 films suffer from the formation of a dense network of cracks much more apparent compared to other films.

Table 1. Rutile phase content and BET surface area (m^2/g) for TiO_2, WO_3, TiO_2/WO_3, $TiO_2/WO_3@Pt$, $H_2:TiO_2/WO_3$, and $H_2:TiO_2/WO_3@Pt$ Thin Films.

	TiO_2	WO_3	TiO_2/WO_3	$TiO_2/WO_3@Pt$	$H_2:TiO_2/WO_3$	$H_2:TiO_2/WO_3@Pt$
Rutile content (%)	7	-	20	19	25	31
S_{BET} ($m^2 g^{-1}$)	78	11	113	109	154	177

Table 2. Transmittance for bare and coated glass; color change ΔE, average roughness (nm), and mean hardness values for titanium specimens coated with TiO_2, WO_3, TiO_2/WO_3, $TiO_2/WO_3@Pt$, $H_2:TiO_2/WO_3$, and $H_2:TiO_2/WO_3@Pt$ Thin Films.

	Substrate	TiO_2	WO_3	TiO_2/WO_3	$TiO_2/WO_3@Pt$	$H_2:TiO_2/WO_3$	$H_2: TiO_2/WO_3@Pt$
Transmittance %	98.1	93.6	85.0	83.9	81.1	77.3	75.8
Delta E	0	0.8	1.3	1.6	1.8	2.1	2.4
Average Roughness (nm)	-	51	40	66	71	108	114
HV_{mean}	-	113	76	148	343	474	635
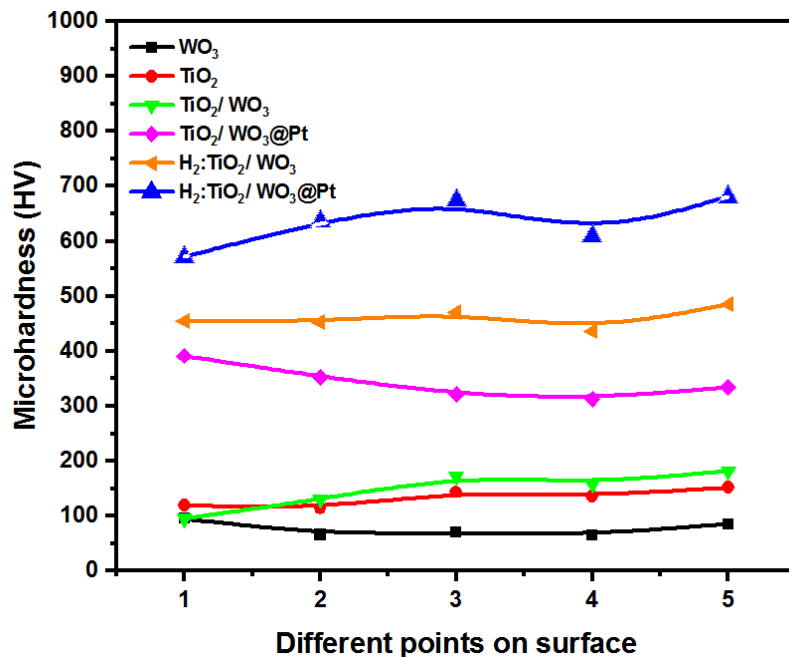
Figure 7. a) Mean value vickers microhardness of titanium coated substrates with WO_3, TiO_2, TiO_2/WO_3, $TiO_2/WO_3@Pt$, $H_2:TiO_2/WO_3$, and $H_2:TiO_2/WO_3@Pt$.

Table 3. OM images (500×) of A) structure of the coated films and B) scratched surfaces (bottom).

WO₃	TiO₂	TiO₂/WO₃	TiO₂/WO₃@Pt	H₂:TiO₂/WO₃	H₂:TiO₂/WO₃@Pt
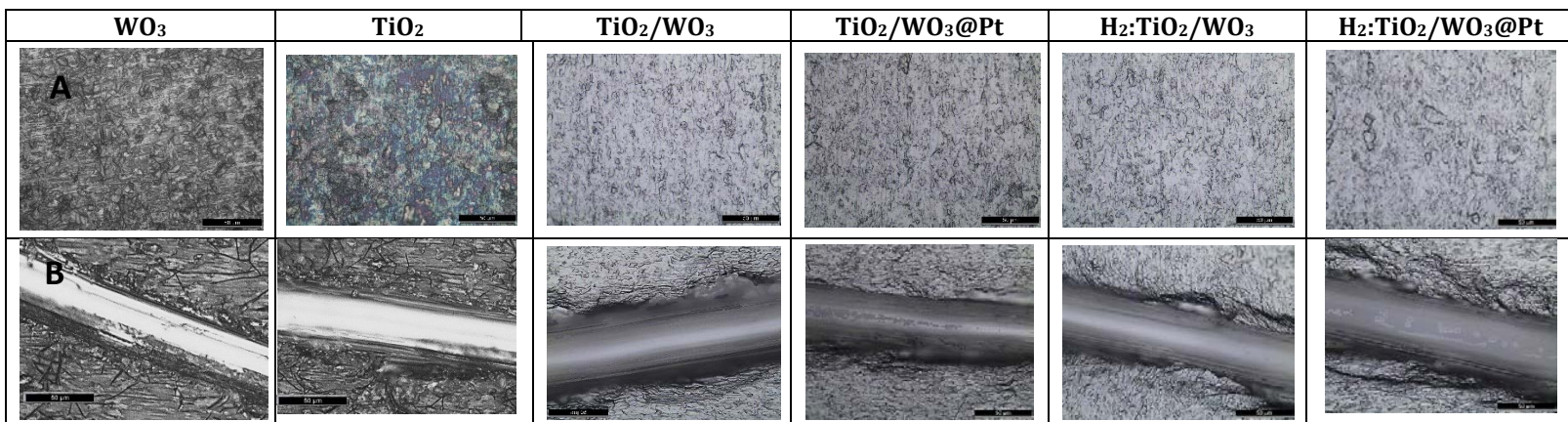
4.2. Photoelectrochemical performance: To study the separation of the electron/hole pairs in the coatings, photocurrent densities were measured under illumination (**Figure 8a** and **Table 4**). $H_2:TiO_2/WO_3@Pt$ generates the highest photocurrent density, which could be ascribed to proper TiO_2 and WO_3 interfacial contacts, rutile fractions in TiO_2, and higher oxygen vacancies amount. The smaller semicircle in the EIS plot of $H_2:TiO_2/WO_3@Pt$ represents the lower charge transfer resistance and efficient separation of electron-hole pairs in this RPC [71],[72], whereas TiO_2 had

a very large arc radius confirming the higher charge transfer (Figure 7b) [73,74]. On the other hand, the positive slope for the samples in Mott–Schottky ($C^{-2}A$–V) plot means that they are all n-type semiconductors (Figure 7c). Moreover, the flat-band potential (V_{fb}) of H_2:TiO_2/WO_3@Pt is lower in comparison to that of other samples (**Table 4**), resulting from a higher carrier concentration and charge transfer on account of higher oxygen vacancies.

The number of donors (N_D) was calculated by equation 1, where e: electronic charge (C), ε_0 : vacuum permittivity (F m^{-1}), ε: relative dielectric constant, C: interfacial capacitance, A: area, ND: number of donors, V: applied voltage, kB: Boltzmann's constant, T: absolute temperature. Values are tabulated in **Table 4**. Accordingly, H_2:TiO_2/WO_3@Pt benefit from a higher N_D, indicating once again an increase in the charge separation performance produced by oxygen vacancies, which leads to a shift of TiO_2 Fermi level towards the CB [75]. Furthermore, the increased electron density in the H_2 treated system facilitates charge separation at the H_2:TiO_2/WO_3@Pt/electrolyte interface.

$$\frac{dC^{-2}}{dV} = -\frac{2}{\varepsilon \varepsilon_o A^2 e N_D} \left(V - V_{fb} - \frac{k_B T}{e} \right) \quad \text{(Equation 1)}$$
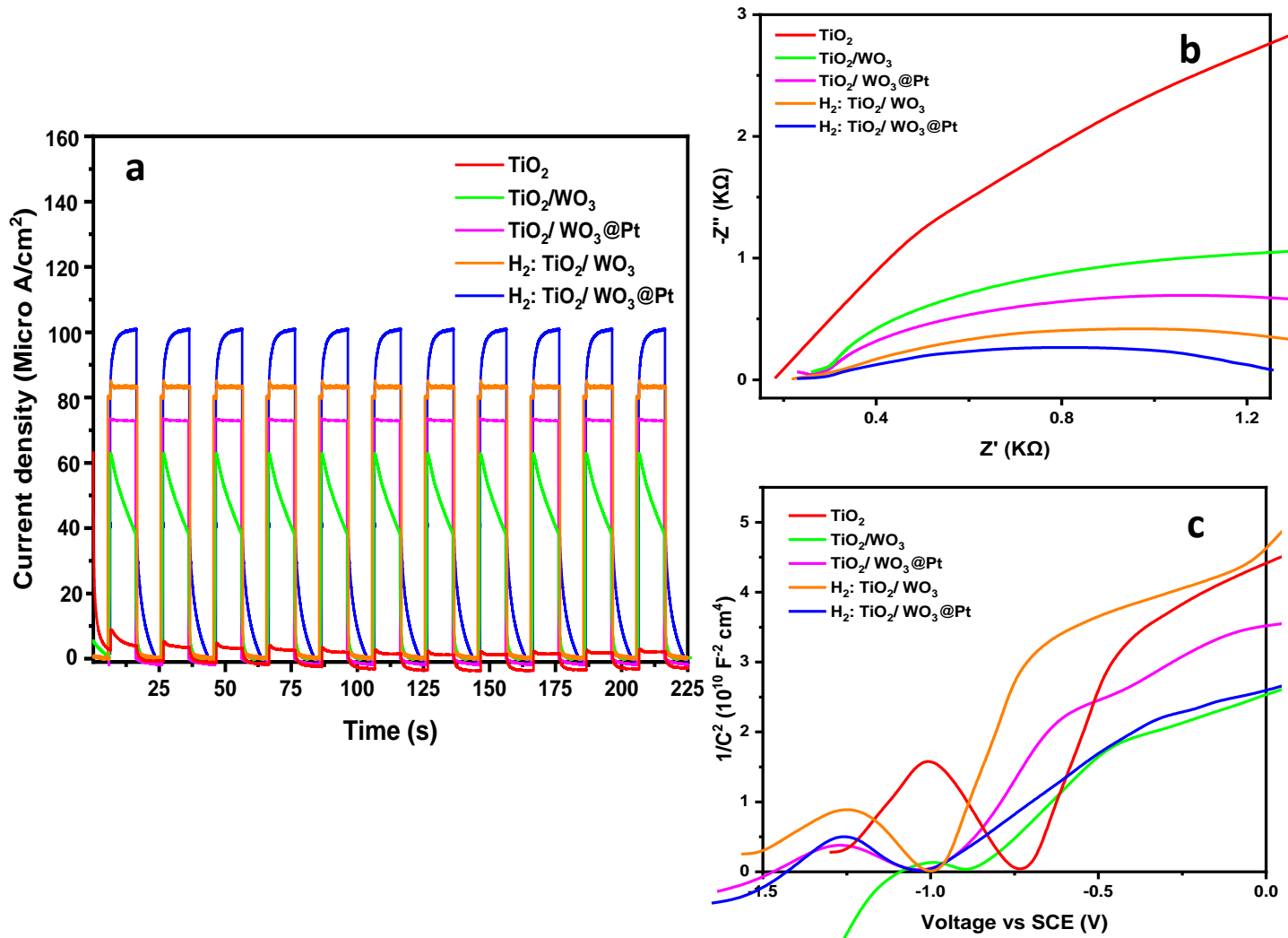
Figure 8. a) Photocurrent response, b) Nyquist plots, and c) Mott-Schottky plots for TiO_2, TiO_2/WO_3, $TiO_2/WO_3@Pt$, $H_2:TiO_2/WO_3$, and $H_2:TiO_2/WO_3@Pt$.

Table 4. Photoelectrochemical properties for TiO_2, TiO_2/WO_3, $TiO_2/WO_3@Pt$, $H_2:TiO_2/WO_3$, and $H_2:TiO_2/WO_3@Pt$.

	TiO_2	TiO_2/WO_3	$TiO_2/WO_3@Pt$	$H_2:TiO_2/WO_3$	$H_2:TiO_2/WO_3@Pt$
Photocurrent density ($\mu A/cm^2$)	6	60	72	84	105
Flat-band potential (V_{fb}) V (versus SCE)	-0.68	-0.84	-0.9	-0.95	-1
Donor density (N_D)	$3.9 * 10^{17}$	$1.1 * 10^{18}$	$1.1 * 10^{18}$	$1.3 * 10^{18}$	$1.5 * 10^{18}$

4.3. Self-cleaning performances and acid rain resistance

4.3.1. Self-cleaning performances: Smart hydrophilic surfaces could clean a surface through a combination of two approaches: (i) wash away dirt on the surface, and (ii) chemically breakdown adsorbed contaminants under sunlight irradiation, exploiting wettability and photocatalytic activity, respectively.

The photocatalytic degradation of MB under UV/visible light and in dark were examined. The obtained results are shown in **Figure 9 a,b and Table 5**. Before light irradiation, the substrates were kept in the dye in dark for 30 min to reach the equilibrium adsorption state. The H_2:TiO_2/WO_3@Pt film shows a significant enhancement towards the photodegradation of MB under both UV and visible lights as well as in dark, as compared to that of other samples. This could be attributed to the stronger light absorption, appropriate anatase/rutile fraction along with enhanced oxygen vacancies. In other words, the H_2:TiO_2/WO_3@Pt RPC film benefits of the synergistic effect of efficient coupling of the two oxides (TiO_2 and WO_3), the addition of Pt nanoparticles, and the introduction of oxygen vacancy defects, thanks to the developed synthetic route which eventually led to improved light absorption and electron storage capacities [76,77].

In detail, during illumination, a part of the electrons is involved in the photodegradation and the remaining electrons are stored in the defective structures of the RPC films; and once the light is turned off, the stored electrons get released and carry on the catalytic reactions. Particularly, the H_2:TiO_2/WO_3@Pt activity in the dark should be related to sufficient charge storage capacity in the defective WO_3 to degrade MB molecules. In this process, the domains of WO_{3-x} on the TiO_{2-y} surface act as acceptor of photo-promoted electrons, increasing charge separation rate.
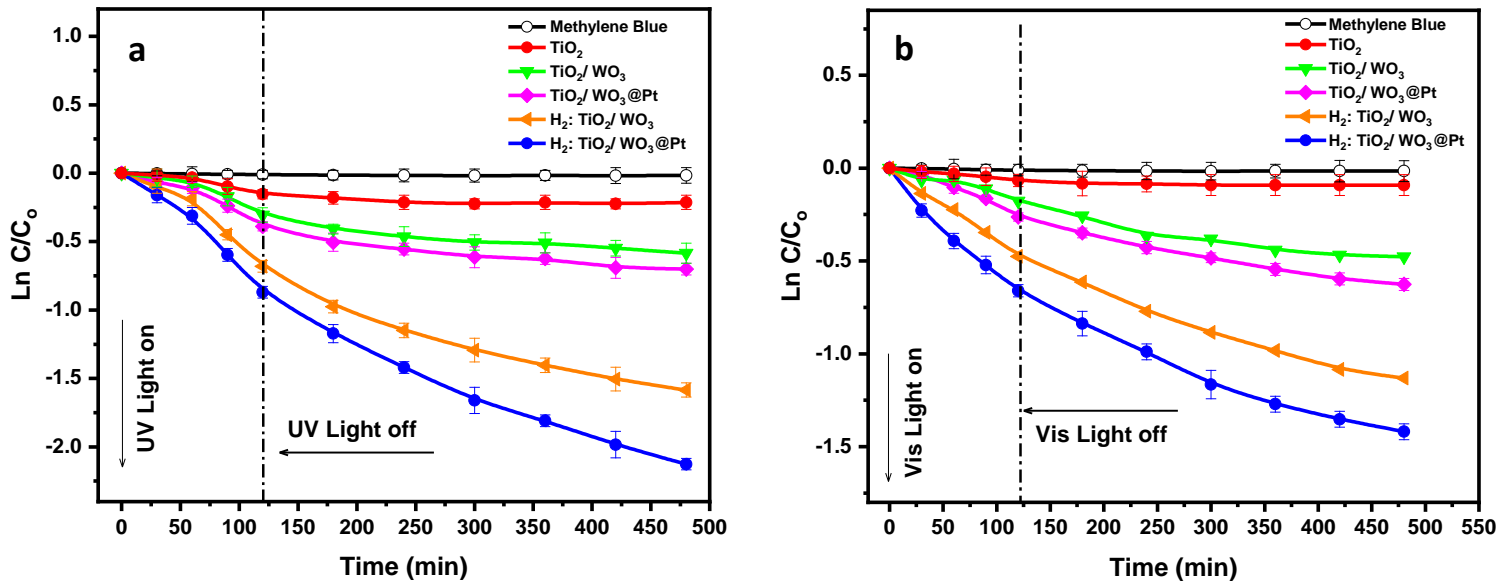
Figure 9. Photo degradation of MB under a) UV and b) visible illuminations for Methylene blue, TiO_2, TiO_2/WO_3, $TiO_2/WO_3@Pt$, $H_2:TiO_2/WO_3$, and $H_2:TiO_2/WO_3@Pt$ coated films.

Table 5. The percent degradation (2 h under light, 6 h in dark) of MB and related kinetic constants under UV and visible illuminations and after light is switched off. n/a = too low to be evaluated

	MB	TiO_2	TiO_2/WO_3	$TiO_2/WO_3@Pt$	$H_2:TiO_2/WO_3$	$H_2:TiO_2/WO_3@Pt$
MB Photodegradation (%)	1.6	19	44	50	75	88
K_{UV} (min^{-1})	n/a	-0.0018	-0.0033	-0.0036	-0.0066	-0.0081
R-Square	0.98	0.95	0.93	0.95	0.96	0.98
$K_{UV\ off}$ (min^{-1})	n/a	-0.0002	-0.0007	-0.0009	-0.0025	-0.0034
R-Square	0.78	0.82	0.91	0.94	0.95	0.98
MB Photodegradation (%)	1.5	8	38	46	62	73
K_{Vis} (min^{-1})	n/a	n/a	-0.0013	-0.0024	-0.0038	-0.0048
R-Square	0.98	0.98	0.85	0.98	0.99	0.99
$K_{Vis\ off}$ (min^{-1})	n/a	n/a	-0.0008	-0.0010	-0.0019	-0.0022
R-Square	0.8	0.82	0.91	0.98	0.97	0.98

Water contact angles (WCA), which depend on the chemical composition of coated materials and structure of the surfaces [78–80], were monitored on the coated surfaces after 24 h storage in the dark, and then under irradiation for 2 h, followed by measurements in the dark for 6 h. All of the coated films except for H_2:TiO_2/WO_3@Pt show initial WCAs above 60 ^{o}; these values for TiO_2 and WO_3 films do not show any significant changing under illumination (**Figure 10** and **Table S2**). However, the addition of WO_3 to TiO_2 decreased WCA in dark and illumination, owing to transfer holes from WO_3 to TiO_2 helping its wettability conversion [81–84]. In the case of H_2:TiO_2/WO_3@Pt this hydrophilic conversion with WCA $_{Dark}$/ WCA $_{light}$: 47 ^{o}: 8 ^{o} is more significant than others. As the light is turned off, all non-hydrogen-treated samples return back to their initial WCA while the ones subjected to hydrogen treatment keep their wettability for hours in the dark, probably due to higher contents of oxygen vacancies resulting from hydrogen treatment [85–87].
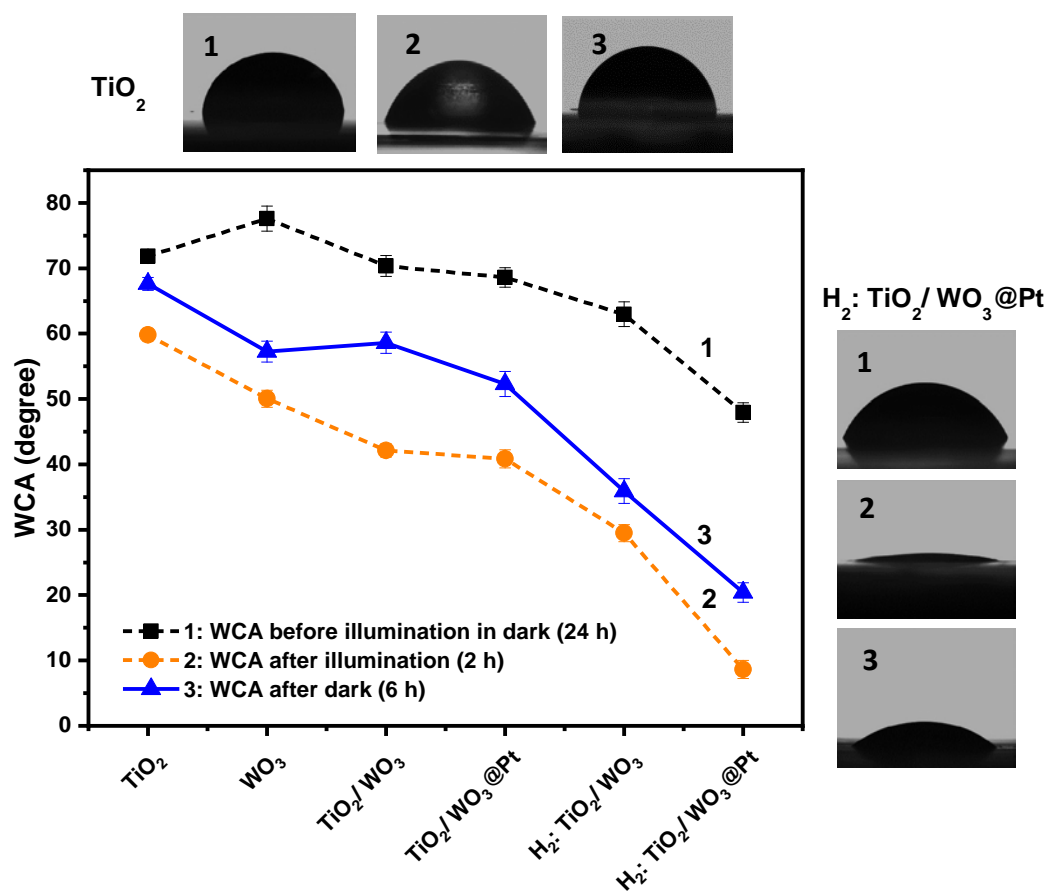
Figure 10. Water contact angle (WCA) of the coated films measured after placing 24 h in dark, and then under irradiation for 2 h following with measurement in dark for 6 h.

4.3.2. Artificial soiling and simulated acid rain tests: The initial color of an artifact could easily be affected by harsh surroundings like acidic media or due to the accumulation of particulate matter suspended in air (i.e. dust, fly ash, soot). Here, we examine the preservation of the coated surface under the artificial tests.

The color change under the artificial soiling test is presented in **Figure 11 a**. Clearly, the coated surfaces present lower ΔE comparing with uncoated one, meaning they underwent limited soiling. Specifically, the H_2:TiO_2/WO_3@Pt RPC coating presents the minimum ΔE in different polluted environments, implying better surface protection than other thin films. These results were expected regarding to the wettability and photoactivity performance of the coatings round the clock, as discussed.

Figure 11 b and **Table 6** show discoloration in the bare and coated substrates affected by the adjusted acidic solution . As expected, the uncoated substrate was strongly discolored with a maximum ΔE around 11 [40]. The specimens coated with TiO_2 and WO_3 showed just a slightly lower ΔE in comparison with the bare surface. However, the ΔE values considerably decreased to below 2 with the H_2:TiO_2/WO_3@Pt coated film, meaning a negligible discoloration.
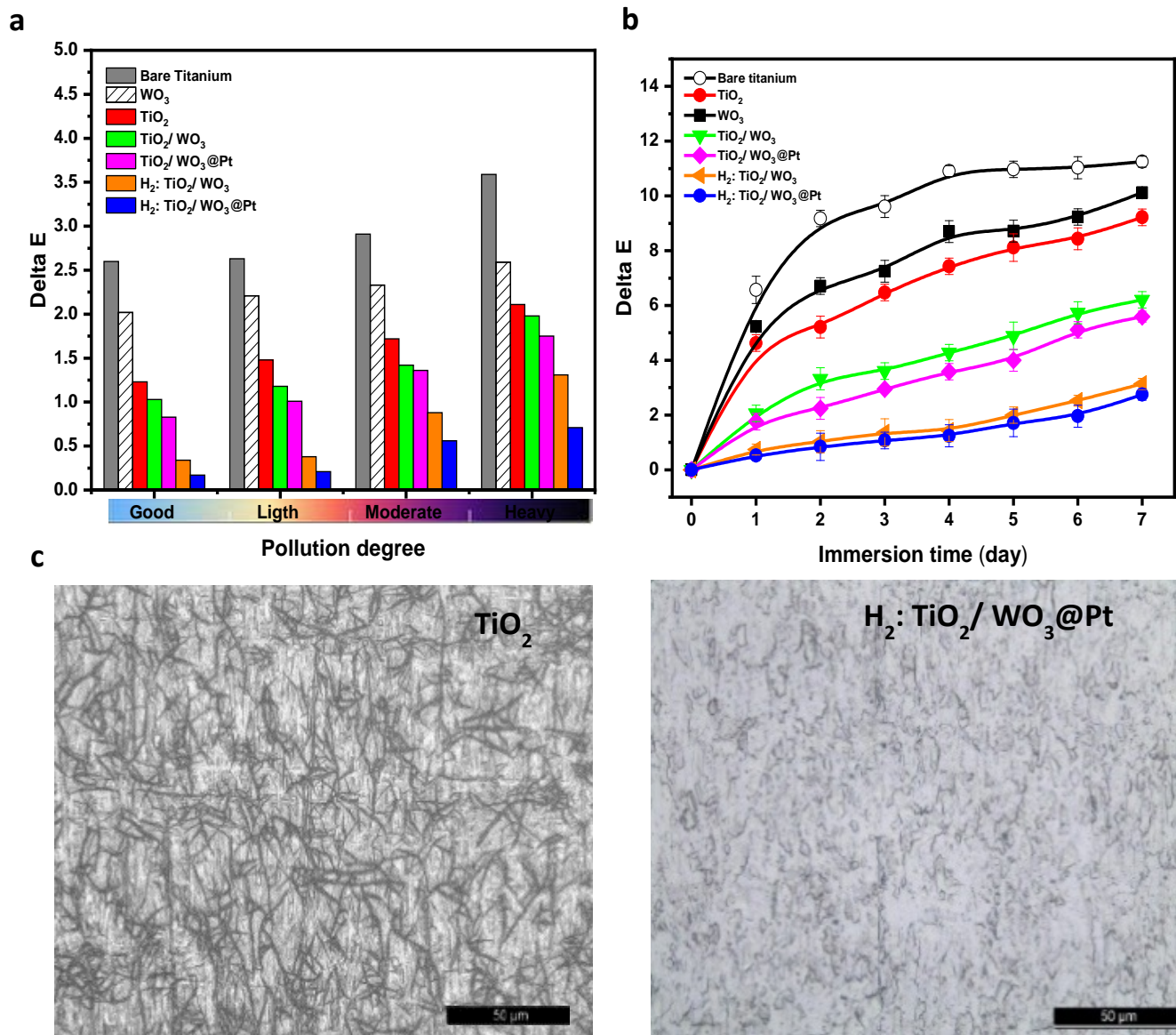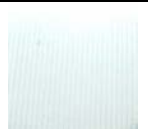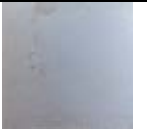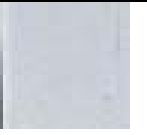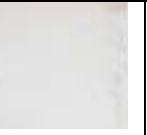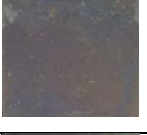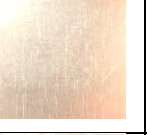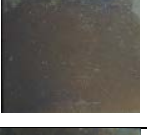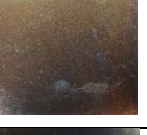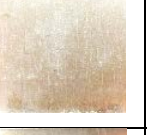
Figure 11. The color difference after a) artificial soiling test mimicking pollution, b) 7 days immersion in an acid solution, and c) OM images of the TiO₂ and H₂: TiO₂/ WO₃@Pt RPC coating's integrity after acid rain aggression.

Table 6. The uncoated and coated specimens affected by the artificial acid rain solution (adjusted at pH 4) after 7 days.

Day	Bare Titanium	TiO$_2$	WO$_3$	TiO$_2$/ WO$_3$	TiO$_2$/ WO$_3$@Pt	H$_2$: TiO$_2$/ WO$_3$	H$_2$: TiO$_2$/ WO$_3$@Pt
0							
1							
2							
3							
4							
5							
6							
7							

The possible coating degradation after artificial acid rain exposure was also evaluated by optical microscopy (**Figure 11c**). While the H$_2$:TiO$_2$/WO$_3$@Pt coating remains unchanged after being in contact with such an aggressive environment, cracks in the TiO$_2$/WO$_3$ and even more in the TiO$_2$ coatings increase remarkably, due to their poor stability. This is in good agreement with weaker mechanical stability and lower hardness of the non-hydrogen treated coatings, resulting from the presence of cracks already in the production stage, in comparison with the crack-free structure of H$_2$:TiO$_2$/WO$_3$@Pt in (see **Figure 7** and **Table 3**).

As the TiO_2 and TiO_2/WO_3 films could not protect the surface from discoloration, the growth of an oxide film as a consequence of titanium oxidation may be responsible for the further damaging of the coatings. On the contrary, the $H_2:TiO_2/WO_3@Pt$ film could protect the surface from color changing and keep its structural integrity after degradation.

4.4. Electron storage ability: To have a better insight about the charge–transport properties of the coatings, electron recombination kinetics of these samples were studied by monitoring the open circuit potential (OCP) versus time upon turning off illumination. In parallel, WCA were also measured at the same time intervals (on different samples produced in identical way) to allow a comparison between wettability alteration and OCP changes. **Figure 12 a** shows the OCP changes versus time for electrodes made from the coatings upon light on/off (active surface area, 6.25 cm^2) and their corresponding WCA. As it can be seen, OCP of TiO_2 electrode decreases from -0.15 to -0.69 V_{SCE} quickly after exposing to light, while it returns to the initial value after turning off the light, which is ascribed to relatively rapid interfacial charge transfer to dissolved O_2 [88]. Clearly, this sample could not store photogenerated charges, as expected given the lack of electron-storing ability of TiO_2. However, OCP increased in the case of the mixed electrodes to -0.55, -0.53, -0.5, and -0.48 V_{SCE} for the TiO_2/WO_3, $TiO_2/WO_3@Pt$, $H_2:TiO_2/WO_3$, and $H_2:TiO_2/WO_3@Pt$, respectively. Furthermore, the $H_2:TiO_2/WO_3@Pt$ anode shows a meaningfully slower OCP decay rate than other samples, indicating effectively retarded recombination of photogenerated charge carriers by the oxygen vacancies [89,90].

The lifetimes of the stored electrons are evaluated by utilizing the off-OCPs (**Figure 12 b**) and the following equation to quantitatively estimate charge storage ability of the samples [91]:

$$\tau = -(\frac{KT}{e})(\frac{dE_{OCP}}{dt})^{-1}$$

where τ: electron lifetime (s), K: Boltzmann constant ($J^{-1}K^{-1}$), T: temperature (K), e: elementary charge (C), E_{ocp}: off-OCP (V), t: time (s). TiO_2/WO_3 shows a lifetime of around 7000 s at -0.41 V_{SCE}, which gradually decreases to 2500 s at -0.24 V_{SCE}, whereas $H_2:TiO_2/WO_3@Pt$ exhibits noticeably higher lifetimes of over 50,000 s at -0.41 V_{SCE} and 12000 s at -0.24 V_{SCE}. These prolonged lifetimes may be ascribed, as abovementioned, to the oxygen vacancies acting as sites

for charge transfer [90]. The effect of these stored and released elections during OCP on WCA of H_2:TiO_2/WO_3@Pt (droplet images in **Figure 12 a**) and illumination and dark time-profiled WCA changes for the samples are presented in **Figure 13**. The WCAs are changed affected by electron charging ability of the coatings under illumination and consequent releasing the stored electrons in dark.

Figure 12. a) The OCP changes versus time with the light on/off (active surface area, 6.25 cm²) for coatings and corresponded WCA images for H₂: TiO₂/ WO₃@Pt, coating film b) Electron lifetimes as a function of OCPs.
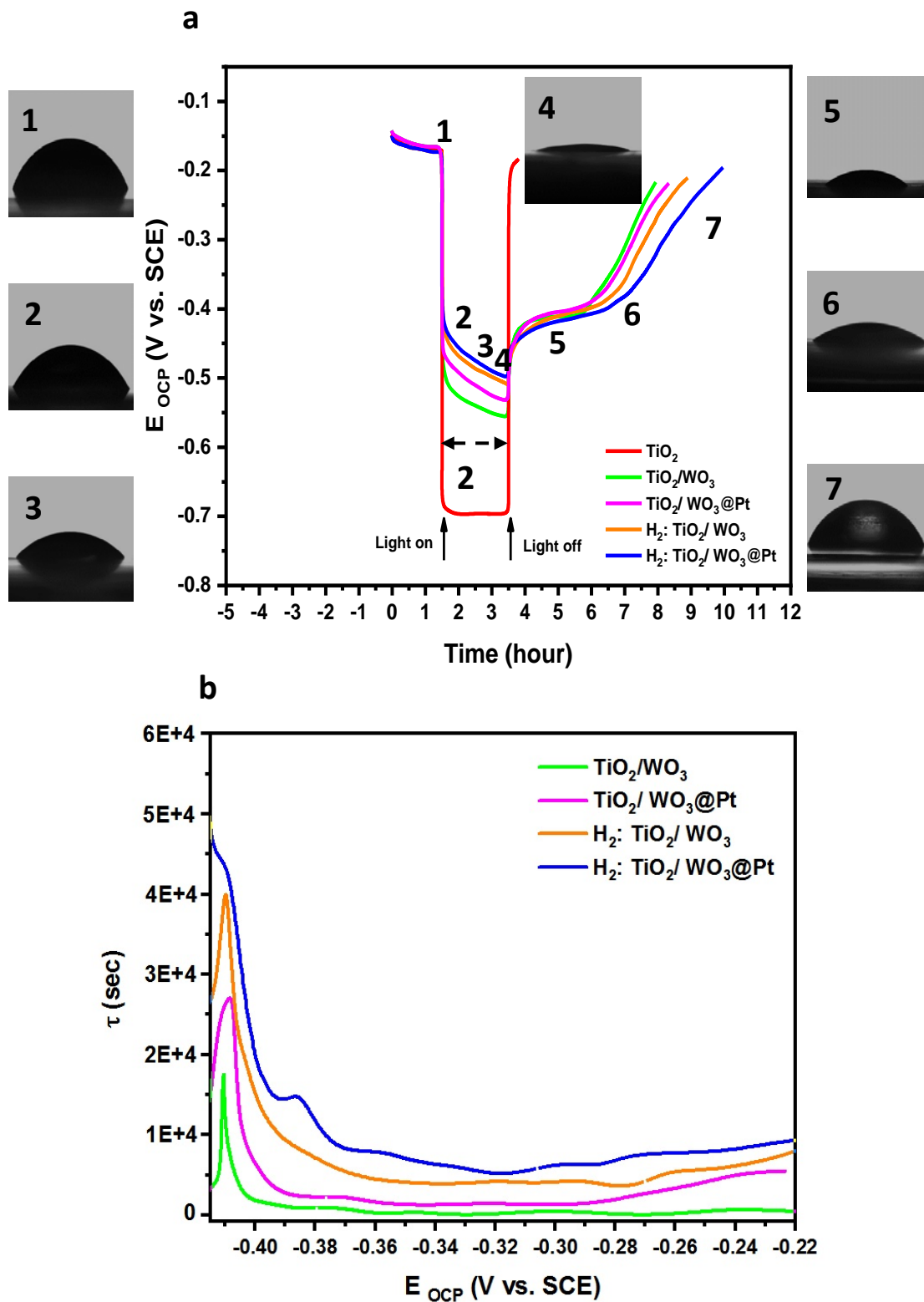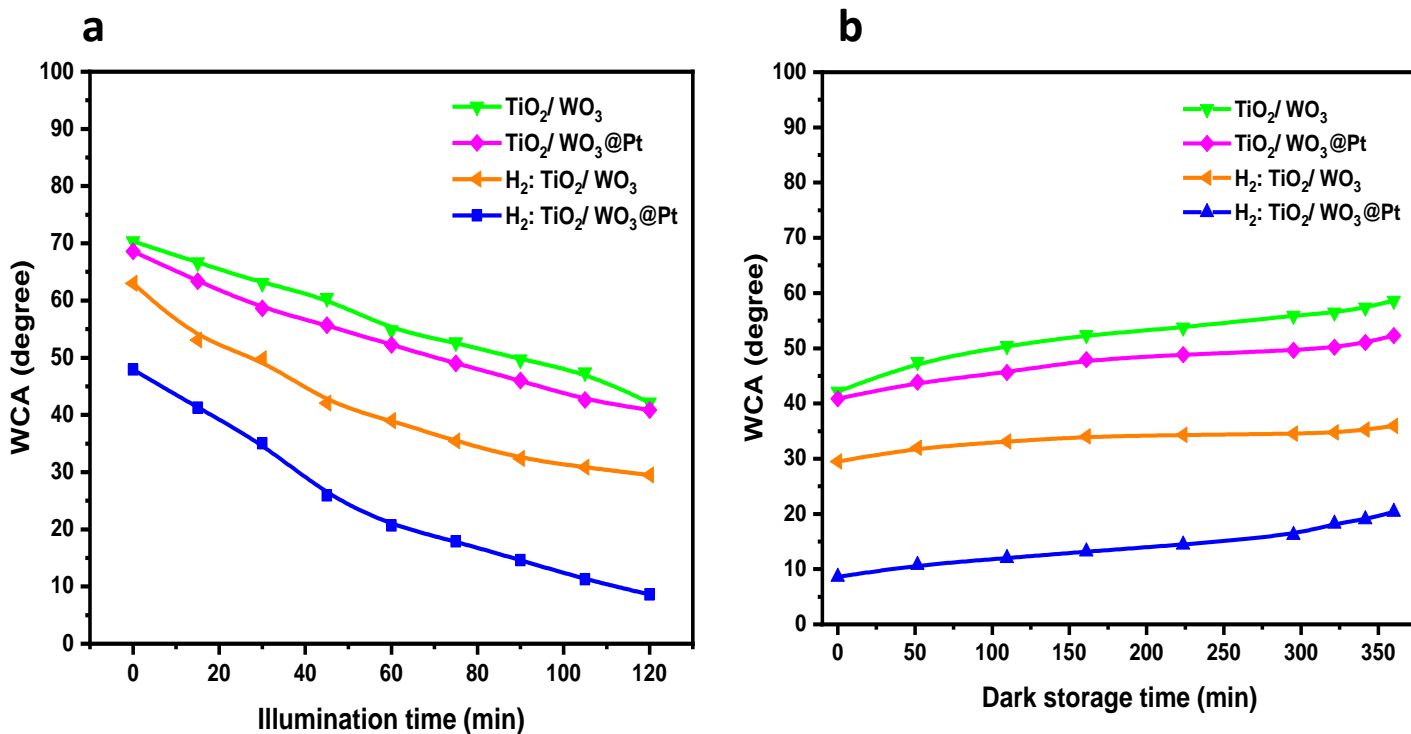
Figure 13. a) illumination, and b) dark storage time-profiled WCA changes for the various coatings.

5. Proposed self-cleaning Mechanism

5.1. Photoactivity mechanism: In **Figure 14,** a suggested mechanism of photocatalytic activity in the H_2:TiO_2/WO_3@Pt RPC composite, is presented schematically as. Results confirm that both oxygen vacancies and Pt cocatalyst play a key role in enhancing charge separations and charge transfer. The presence of Pt nanoparticles induces efficient electron transfer to different sites. Thus, more holes can take part in the MB photodegradation. Additionally, oxygen reduction could be facilitated over Pt, improving contaminants photodegradation. In contrast, oxygen vacancies formed in WO_3 by H_2 treatment induce the formation of defective band structures in WO_3. These defect bands can make an upshift in the Fermi level resulting in more available trapping sites for the storage of electrons, for a more efficient round-the-clock photoactivity.
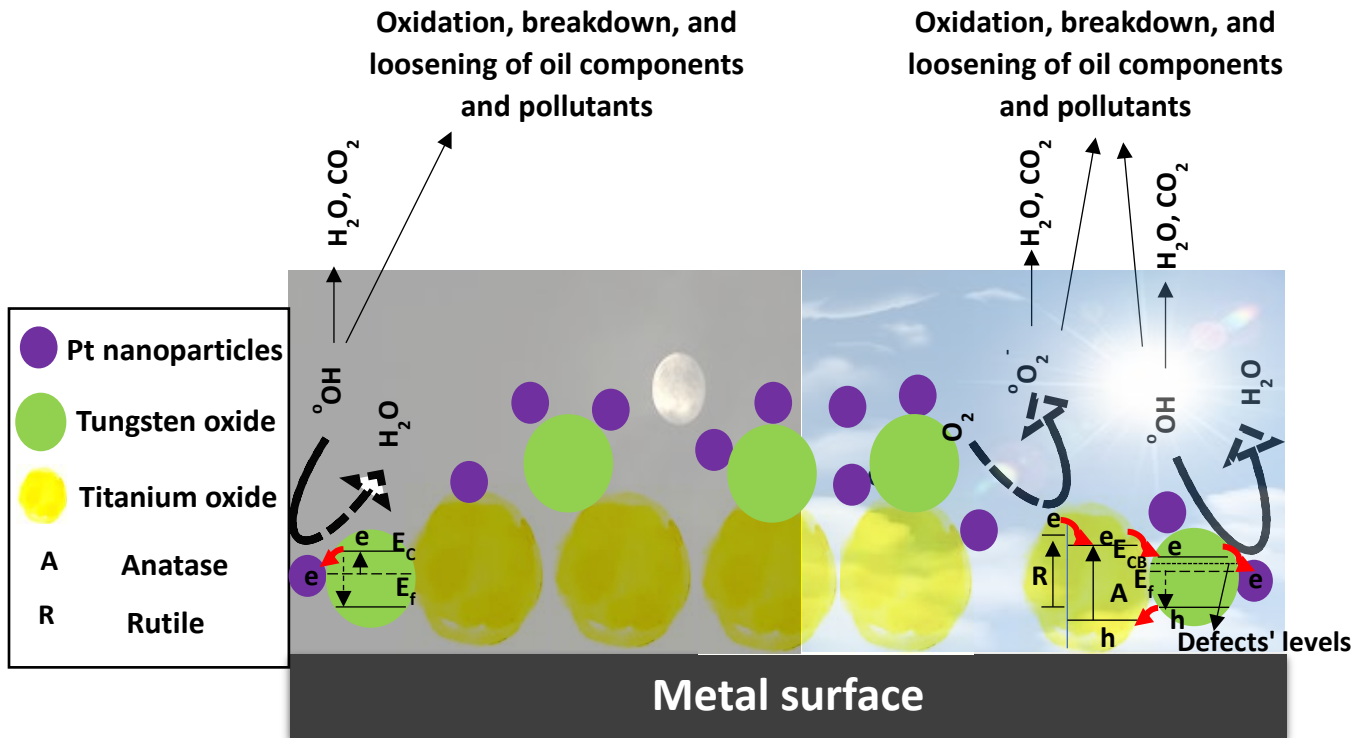
Figure 14. Schematic illustration of the 24-working catalytic mechanism in the H_2:TiO_2/WO_3@Pt RPC coated substrate.

5.2. Hydrophilicity mechanism: It is confirmed that water molecules coming from atmospheric humidity or rain droplets can capture oxygen vacancy sites leading to form hydroxyl groups on the H_2:TiO_2/WO_3@Pt RPC surface, due to the transfer of one proton from the water molecule to a close oxygen atom of the surface, producing two hydroxyl groups for each vacancy [87].Interaction between these hydroxyl groups with water molecules can form hydrogen bonds, which switches the surface towards more hydrophilic behavior (**Figure 15**).
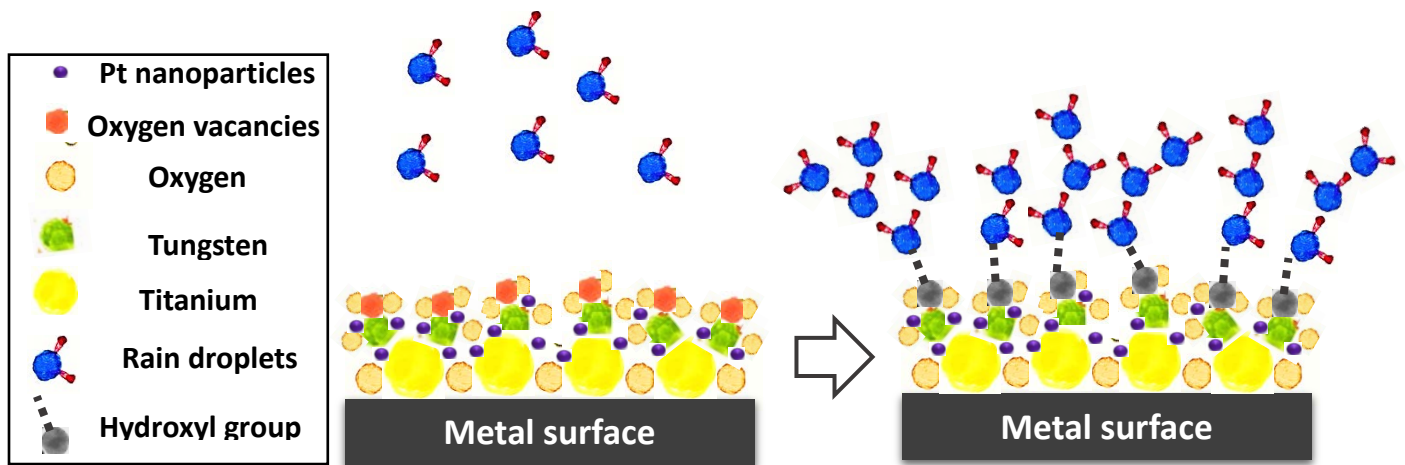
Figure 15. Schematic diagram of proposed wettability mechanism showing rain droplet adoption on H$_2$:TiO$_2$/WO$_3$@Pt RPC surface.

Conclusion

In this work we have successfully fabricated a high surface area day-night self-cleaning coating, consisting of hydrogen-treated, Pt decorated mixed oxides (TiO$_2$/WO$_3$) produced through soft templating approach. This transparent coating showed proper adhesion, integrity excellent photoactivity and wettability both under light and in darkness: all these properties contributed to an excellent behavior in self-cleaning applications, in terms of substrate protection from both soiling and degradation induced by the contact with polluted atmospheres. The high photoactivity for contaminants degradation under resulted from the synergistic effects of Pt co-catalyst, oxygen vacancies, improved surface area and optimal TiO$_2$/WO$_3$ interfacial contact. Furthermore, the smart surface could maintain the substrate clean by benefiting from superhydrophilic properties, which were maintained for hours in the dark due to its round-the-clock activity, promoted by WO$_3$ electron storage and accentuated by the presence of oxygen vacancies.

References

[1]   M. Mokhtarifar, M.P. Pedeferri, M.V. Diamanti, Towards a better preservation of current

and future outdoor architectural heritage; maximum suppression of discolouration in anodized and non-anodized titanium sheets, Environ. Technol. Rev. (2020). https://doi.org/10.1080/21622515.2020.1732480.

[2]   E. Gaul, Coloring titanium and related metals by electrochemical oxidation, J. Chem. Educ. (1993). https://doi.org/10.1021/ed070p176.

[3]   M. V. Diamanti, S. Codeluppi, A. Cordioli, M.P. Pedeferri, Effect of thermal oxidation on titanium oxides' characteristics, J. Exp. Nanosci. (2009). https://doi.org/10.1080/17458080902769937.

[4]   M. V. Diamanti, B. Del Curto, V. Masconale, C. Passaro, M.P. Pedeferri, Anodic coloring of titanium and its alloy for jewels production, Color Res. Appl. (2012). https://doi.org/10.1002/col.20683.

[5]   K. Takahashi, M. Kaneko, T. Hayashi, I. Muto, J. Tamenari, K. Tokuno, Improvement of discoloration resistance of vacuum annealed commercially pure titanium sheets in atmospheric environments, Tetsu-To-Hagane/Journal Iron Steel Inst. Japan. 90 (2004) 278–285. https://doi.org/10.2355/tetsutohagane1955.90.5_278.

[6]   M. Kaneko, K. Takahashi, T. Hayashi, K. Tokuno, J. Tamenari, Discoloration resistance of architectural titanium sheets in long-term atmospheric exposure tests, Mater. Perform. 45 (2006) 38–42.

[7]   E.M. Szesz, B.L. Pereira, N.K. Kuromoto, C.E.B. Marino, G.B. De Souza, P. Soares, Electrochemical and morphological analyses on the titanium surface modified by shot blasting and anodic oxidation processes, in: Thin Solid Films, 2013. https://doi.org/10.1016/j.tsf.2012.09.096.

[8]   R. Supplit, T. Koch, U. Schubert, Evaluation of the anti-corrosive effect of acid pickling and sol-gel coating on magnesium AZ31 alloy, Corros. Sci. (2007). https://doi.org/10.1016/j.corsci.2007.02.006.

[9]   R.T. Pelegrini, R.S. Freire, N. Duran, R. Bertazzoli, Photoassisted electrochemical degradation of organic pollutants on a DSA type oxide electrode: process test for a phenol synthetic solution and its application for the E1 bleach kraft mill effluent, Environ. Sci. Technol. 35 (2001) 2849–2853.

[10]   M.S. Vohra, K. Tanaka, Photocatalytic degradation of aqueous pollutants using silica-modified TiO2, Water Res. 37 (2003) 3992–3996. https://doi.org/10.1016/S0043-1354(03)00333-6.

[11]   M. Hepel, J. Luo, Photoelectrochemical mineralization of textile diazo dye pollutants using nanocrystalline WO3 electrodes, Electrochim. Acta. 47 (2001) 729–740. https://doi.org/10.1016/S0013-4686(01)00753-8.

[12]   T. Pauporté, J. Rathouský, Electrodeposited mesoporous ZnO thin films as efficient photocatalysts for the degradation of dye pollutants, J. Phys. Chem. C. 111 (2007) 7639–7644. https://doi.org/10.1021/jp071465f.

[13]   Y. Wei, J. Wang, R. Yu, J. Wan, D. Wang, Constructing SrTiO$_3$-TiO$_2$ Heterogeneous

Hollow Multi-shelled Structures for Enhanced Solar Water Splitting, Angew. Chemie. (2018). https://doi.org/10.1002/ange.201812364.

[14] T. Tatsuma, S. Saitoh, Y. Ohko, A. Fujishima, TiO2-WO3 photoelectrochemical anticorrosion system with an energy storage ability, Chem. Mater. (2001). https://doi.org/10.1021/cm010024k.

[15] T. Tatsuma, S. Saitoh, P. Ngaotrakanwiwat, Y. Ohko, A. Fujishima, Energy storage of TiO2-WO3 photocatalysis systems in the gas phase, Langmuir. 18 (2002) 7777–7779. https://doi.org/10.1021/la026011i.

[16] P. Ngaotrakanwiwat, T. Tatsuma, S. Saitoh, Y. Ohko, A. Fujishima, Charge-discharge behavior of TiO2-WO3 photocatalysis systems with energy storage ability, Phys. Chem. Chem. Phys. (2003). https://doi.org/10.1039/b304181f.

[17] T. Tatsuma, S. Takeda, S. Saitoh, Y. Ohko, A. Fujishima, Bactericidal effect of an energy storage TiO2-WO3 photocatalyst in dark, Electrochem. Commun. (2003). https://doi.org/10.1016/j.elecom.2003.07.003.

[18] X. Sun, Y. Guo, C. Wu, Y. Xie, The Hydric Effect in Inorganic Nanomaterials for Nanoelectronics and Energy Applications, Adv. Mater. 27 (2015) 3850–3867. https://doi.org/10.1002/adma.201500546.

[19] L. Zhang, S. Wang, C. Lu, Detection of Oxygen Vacancies in Oxides by Defect-Dependent Cataluminescence, Anal. Chem. (2015). https://doi.org/10.1021/acs.analchem.5b02267.

[20] J. Tian, Z. Zhao, A. Kumar, R.I. Boughton, H. Liu, Recent progress in design, synthesis, and applications of one-dimensional TiO2 nanostructured surface heterostructures: A review, Chem. Soc. Rev. (2014). https://doi.org/10.1039/c4cs00180j.

[21] C.C. Nguyen, N.N. Vu, T.O. Do, Efficient hollow double-shell photocatalysts for the degradation of organic pollutants under visible light and in darkness, J. Mater. Chem. A. (2016). https://doi.org/10.1039/c5ta09016d.

[22] Q. Liu, F. Wang, H. Lin, Y. Xie, N. Tong, J. Lin, X. Zhang, Z. Zhang, X. Wang, Surface oxygen vacancy and defect engineering of WO3 for improved visible light photocatalytic performance, Catal. Sci. Technol. (2018). https://doi.org/10.1039/c8cy00994e.

[23] M.R. Bayati, F. Golestani-Fard, A.Z. Moshfegh, Visible photodecomposition of methylene blue over micro arc oxidized WO3-loaded TiO2 nano-porous layers, Appl. Catal. A Gen. 382 (2010) 322–331. https://doi.org/10.1016/j.apcata.2010.05.017.

[24] Y. Li, G. Chen, Q. Wang, X. Wang, A. Zhou, Z. Shen, Hierarchical ZnS-In2 S3 -CuS nanospheres with nanoporous structure: Facile synthesis, growth mechanism, and excellent photocatalytic activity, Adv. Funct. Mater. (2010). https://doi.org/10.1002/adfm.201000604.

[25] X. Pan, M.Q. Yang, X. Fu, N. Zhang, Y.J. Xu, Defective TiO2 with oxygen vacancies: Synthesis, properties and photocatalytic applications, Nanoscale. (2013). https://doi.org/10.1039/c3nr00476g.

[26]   C.C. Nguyen, N.N. Vu, S. Chabot, S. Kaliaguine, T.O. Do, Role of CxNy-Triazine in Photocatalysis for Efficient Hydrogen Generation and Organic Pollutant Degradation Under Solar Light Irradiation, Sol. RRL. (2017). https://doi.org/10.1002/solr.201700012.

[27]   J. Zhao, X. Wang, Z. Xu, J.S.C. Loo, Hybrid catalysts for photoelectrochemical reduction of carbon dioxide: A prospective review on semiconductor/metal complex co-catalyst systems, J. Mater. Chem. A. (2014). https://doi.org/10.1039/c4ta02250e.

[28]   A. Meng, J. Zhang, D. Xu, B. Cheng, J. Yu, Enhanced photocatalytic H2-production activity of anatase TiO2 nanosheet by selectively depositing dual-cocatalysts on (101) and (001) facets, Appl. Catal. B Environ. 198 (2016) 286–294. https://doi.org/10.1016/j.apcatb.2016.05.074.

[29]   D.T. Nguyen, C.C. Nguyen, M. St-Jean, S. Chabot, S. Kaliaguine, T.O. Do, All in One: Contributions of Ni Dopants and Ni/NiS Dual Cocatalysts to the Enhanced Efficiency of TiO2 Photocatalyst for the Degradation of Organic Pollutants, ACS Appl. Nano Mater. (2018). https://doi.org/10.1021/acsanm.8b01693.

[30]   S.J. Weinstein, K.J. Ruschak, Dip coating on a planar non-vertical substrate in the limit of negligible surface tension, Chem. Eng. Sci. (2001). https://doi.org/10.1016/S0009-2509(01)00147-6.

[31]   Z. Hu, J. Zhang, S. Xiong, Y. Zhao, Annealing-free, air-processed and high-efficiency polymer solar cells fabricated by a dip coating process, Org. Electron. (2012). https://doi.org/10.1016/j.orgel.2011.09.026.

[32]   N. Rajabi, F. Heshmatpour, R. Malekfar, H.R. Bahari-Poor, S. Abyar, A comparative study of dip coating and spray pyrolysis methods for synthesizing ITO nanolayers by using Ag colloidal sol, Mater. Sci. Pol. (2014). https://doi.org/10.2478/s13536-013-0165-x.

[33]   D. Grosso, How to exploit the full potential of the dip-coating process to better control film formation, J. Mater. Chem. (2011). https://doi.org/10.1039/c1jm12837j.

[34]   M. Faustini, B. Louis, P.A. Albouy, M. Kuemmel, D. Grosso, Preparation of sol-gel films by dip-coating in extreme conditions, J. Phys. Chem. C. (2010). https://doi.org/10.1021/jp9114755.

[35]   M. Guglielmi, P. Colombo, F. Peron, L. Mancinelli Degli Esposti, Dependence of thickness on the withdrawal speed for SiO2 and TiO2 coatings obtained by the dipping method, J. Mater. Sci. (1992). https://doi.org/10.1007/BF01105273.

[36]   D.R. Ceratti, B. Louis, X. Paquez, M. Faustini, D. Grosso, A New Dip Coating Method to Obtain Large-Surface Coatings with a Minimum of Solution, Adv. Mater. (2015). https://doi.org/10.1002/adma.201502518.

[37]   T. Bottein, J. Loizillon, D. Grosso, Full Investigation of Angle Dependence in Dip-Coating Sol-Gel Films, J. Phys. Chem. B. (2017). https://doi.org/10.1021/acs.jpcb.7b04122.

[38]   M. Bagherzadeh, R. Kaveh, A new SnS2-BiFeO3/reduced graphene oxide photocatalyst with superior photocatalytic capability under visible light irradiation, J. Photochem.

Photobiol. A Chem. 359 (2018) 11–22. https://doi.org/10.1016/j.jphotochem.2018.03.031.

[39]   M. Bagherzadeh, R. Kaveh, S. Ozkar, S. Akbayrak, Preparation and characterization of a new CdS–NiFe2O4/reduced graphene oxide photocatalyst and its use for degradation of methylene blue under visible light irradiation, Res. Chem. Intermed. 44 (2018) 5953–5979. https://doi.org/10.1007/s11164-018-3466-1.

[40]   M. Mokhtarifar, R. Kaveh, M. Bagherzadeh, A. Lucotti, M.P. Pedeferri, M.V. Diamanti, Heterostructured TiO2/SiO2/γ-Fe2O3/rGO Coating with Highly Efficient Visible-Light-Induced Self-Cleaning Properties for Metallic Artifacts, ACS Appl. Mater. Interfaces. (2020). https://doi.org/10.1021/acsami.0c06792.

[41]   M. Mokhtarifar, R. Kaveh, M. Ormellese, M. Bagherzadeh, M.V. Diamanti, M. Pedeferri, On the role of γ-fe2 o3 nanoparticles and reduced graphene oxide nanosheets in enhancing self-cleaning properties of composite tio2 for cultural heritage protection, Coatings. (2020). https://doi.org/10.3390/coatings10100933.

[42]   H.G. Yang, C.H. Sun, S.Z. Qiao, J. Zou, G. Liu, S.C. Smith, H.M. Cheng, G.Q. Lu, Anatase TiO2 single crystals with a large percentage of reactive facets, Nature. (2008). https://doi.org/10.1038/nature06964.

[43]   J. Beyer, A. Mamakhel, F. Søndergaard-Pedersen, J. Yu, B.B. Iversen, Continuous flow hydrothermal synthesis of phase pure rutile TiO2 nanoparticles with a rod-like morphology, Nanoscale. (2020). https://doi.org/10.1039/c9nr09069j.

[44]   Q. Zhang, L. Gao, J. Guo, Effects of calcination on the photocatalytic properties of nanosized TiO2 powders prepared by TiCl4 hydrolysis, Appl. Catal. B Environ. 26 (2000) 207–215. https://doi.org/10.1016/S0926-3373(00)00122-3.

[45]   Y. Li, Y. Fan, Y. Chen, A novel method for preparation of nanocrystalline rutile TiO2 powders by liquid hydrolysis of TiCl4, J. Mater. Chem. 12 (2002) 1387–1390. https://doi.org/10.1039/b200018k.

[46]   Z. Zhu, X. He, Y. Zhao, Q. Ren, Influence of WO3 additive on crystallite structural transformation of TiO2 powders, Xiyou Jinshu Cailiao Yu Gongcheng/Rare Met. Mater. Eng. 39 (2010) 771–774. https://doi.org/10.1016/s1875-5372(10)60099-9.

[47]   N. Couselo, F.S. García Einschlag, R.J. Candal, M. Jobbágy, Tungsten-doped TiO2 vs pure TiO2 photocatalysts: Effects on photobleaching kinetics and mechanism, J. Phys. Chem. C. 112 (2008) 1094–1100. https://doi.org/10.1021/jp0769781.

[48]   S. Patra, C. Andriamiadamanana, M. Tulodziecki, C. Davoisne, P.L. Taberna, F. Sauvage, Low-temperature electrodeposition approach leading to robust mesoscopic anatase TiO2 films, Sci. Rep. 6 (2016). https://doi.org/10.1038/srep21588.

[49]   X.Z. Li, F.B. Li, C.L. Yang, W.K. Ge, Photocatalytic activity of WOx-TiO2 under visible light irradiation, J. Photochem. Photobiol. A Chem. 141 (2001) 209–217. https://doi.org/10.1016/S1010-6030(01)00446-4.

[50]   S. Djerad, L. Tifouti, M. Crocoll, W. Weisweiler, Effect of vanadia and tungsten loadings on the physical and chemical characteristics of V2O5-WO3/TiO2 catalysts, J. Mol. Catal. A Chem. 208 (2004) 257–265. https://doi.org/10.1016/j.molcata.2003.07.016.

[51] G. Ren, Y. Gao, J. Yin, A. Xing, H. Liu, Synthesis of high-activity TiO2/WO3 photocatalyst via environmentally friendly and microwave assisted hydrothermal process, J. Chem. Soc. Pakistan. 33 (2011) 666–670.

[52] P.M. Woodward, A.W. Sleight, T. Vogt, Ferroelectric Tungsten Trioxide, J. Solid State Chem. (1997). https://doi.org/10.1006/jssc.1997.7268.

[53] K. Thummavichai, N. Wang, F. Xu, G. Rance, Y. Xia, Y. Zhu, In situ investigations of the phase change behaviour of tungsten oxide nanostructures, R. Soc. Open Sci. (2018). https://doi.org/10.1098/rsos.171932.

[54] R.S. Vemuri, K.K. Bharathi, S.K. Gullapalli, C. V. Ramana, Effect of structure and size on the electrical properties of nanocrystalline WO3 films, ACS Appl. Mater. Interfaces. (2010). https://doi.org/10.1021/am1004514.

[55] M. Govender, B.W. Mwakikunga, A.G.J. Machatine, H.W. Kunert, Electrical and optical properties of mixed phase tungsten trioxide films grown by laser pyrolysis, Phys. Status Solidi Curr. Top. Solid State Phys. (2014). https://doi.org/10.1002/pssc.201300212.

[56] S. Pokhrel, J. Birkenstock, A. Dianat, J. Zimmermann, M. Schowalter, A. Rosenauer, L.C. Ciacchi, L. Mädler, In situ high temperature X-ray diffraction, transmission electron microscopy and theoretical modeling for the formation of WO3 crystallites, CrystEngComm. (2015). https://doi.org/10.1039/c5ce00526d.

[57] A.K. Battu, S. Manandhar, C. V. Ramana, Molybdenum Incorporation Induced Enhancement in the Mechanical Properties of Gallium Oxide Films, Adv. Mater. Interfaces. (2017). https://doi.org/10.1002/admi.201700378.

[58] W.C. Conner, J.L. Falconer, Spillover in Heterogeneous Catalysis, Chem. Rev. (1995). https://doi.org/10.1021/cr00035a014.

[59] M. Catauro, E. Tranquillo, G. Dal Poggetto, M. Pasquali, A. Dell'Era, S.V. Ciprioti, Influence of the heat treatment on the particles size and on the crystalline phase of TiO2 synthesized by the sol-gel method, Materials (Basel). (2018). https://doi.org/10.3390/ma11122364.

[60] C. Su, B.Y. Hong, C.M. Tseng, Sol-gel preparation and photocatalysis of titanium dioxide, in: Catal. Today, 2004. https://doi.org/10.1016/j.cattod.2004.06.132.

[61] T.D. Nguyen-Phan, S. Luo, Z. Liu, A.D. Gamalski, J. Tao, W. Xu, E.A. Stach, D.E. Polyansky, S.D. Senanayake, E. Fujita, J.A. Rodriguez, Striving Toward Noble-Metal-Free Photocatalytic Water Splitting: The Hydrogenated-Graphene-TiO2 Prototype, Chem. Mater. (2015). https://doi.org/10.1021/acs.chemmater.5b02131.

[62] J.Y. Eom, S.J. Lim, S.M. Lee, W.H. Ryu, H.S. Kwon, Black titanium oxide nanoarray electrodes for high rate Li-ion microbatteries, J. Mater. Chem. A. (2015). https://doi.org/10.1039/c5ta01718a.

[63] R. Wu, J. Zhang, Y. Shi, D. Liu, B. Zhang, Metallic WO2-Carbon Mesoporous Nanowires as Highly Efficient Electrocatalysts for Hydrogen Evolution Reaction, J. Am. Chem. Soc. (2015). https://doi.org/10.1021/jacs.5b01330.

[64]   J. Yan, T. Wang, G. Wu, W. Dai, N. Guan, L. Li, J. Gong, Tungsten oxide single crystal nanosheets for enhanced multichannel solar light harvesting, Adv. Mater. (2015). https://doi.org/10.1002/adma.201404792.

[65]   Y. Wei, J. Xu, H. Dong, J.H. Dong, K. Qiu, S.A. Jansen-Varnum, Preparation and physisorption characterization of D-glucose-templated mesoporous silica sol-gel materials, Chem. Mater. 11 (1999) 2023–2029. https://doi.org/10.1021/cm981004u.

[66]   N. Serpone, Heterogeneous photocatalysis and prospects of TiO2-based photocatalytic DeNOxing the atmospheric environment, Catalysts. 8 (2018). https://doi.org/10.3390/catal8110553.

[67]   Y. Cao, X. Li, Z. Bian, A. Fuhr, D. Zhang, J. Zhu, Highly photocatalytic activity of brookite/rutile TiO2 nanocrystals with semi-embedded structure, Appl. Catal. B Environ. 180 (2016) 551–558. https://doi.org/10.1016/j.apcatb.2015.07.003.

[68]   S. Vepřek, S. Reiprich, A concept for the design of novel superhard coatings, Thin Solid Films. (1995). https://doi.org/10.1016/0040-6090(95)06695-0.

[69]   E. Lugscheider, O. Knotek, K. Bobzin, S. Bärwulf, Tribological properties, phase generation and high temperature phase stability of tungsten- and vanadium-oxides deposited by reactive MSIP-PVD process for innovative lubrication applications, Surf. Coatings Technol. (2000). https://doi.org/10.1016/S0257-8972(00)00963-4.

[70]   O. Zywitzki, T. Modes, H. Sahm, P. Frach, K. Goedicke, D. Glöß, Structure and properties of crystalline titanium oxide layers deposited by reactive pulse magnetron sputtering, Surf. Coatings Technol. (2004). https://doi.org/10.1016/j.surfcoat.2003.10.115.

[71]   W.H. Leng, Z. Zhang, J.Q. Zhang, C.N. Cao, Investigation of the kinetics of a TiO2 photoelectrocatalytic reaction involving charge transfer and recombination through surface states by electrochemical impedance spectroscopy, J. Phys. Chem. B. (2005). https://doi.org/10.1021/jp051821z.

[72]   N. Baram, Y. Ein-eli, Electrochemical Impedance Spectroscopy of Porous TiO 2 for Photocatalytic Applications, J. Phys. Chem. C. 2 (2010) 9781–9790. https://doi.org/10.1021/jp911687w.

[73]   B.L. He, B. Dong, H.L. Li, Preparation and electrochemical properties of Ag-modified TiO2 nanotube anode material for lithium-ion battery, Electrochem. Commun. 9 (2007) 425–430. https://doi.org/10.1016/j.elecom.2006.10.008.

[74]   H. Zhang, X. Lv, Y. Li, Y. Wang, J. Li, P25-graphene composite as a high performance photocatalyst, ACS Nano. 4 (2010) 380–386. https://doi.org/10.1021/nn901221k.

[75]   D.C. Cronemeyer, Infrared absorption of reduced rutile TiO2 single crystals, Phys. Rev. (1959). https://doi.org/10.1103/PhysRev.113.1222.

[76]   H. Park, Y. Park, W. Kim, W. Choi, Surface modification of TiO2 photocatalyst for environmental applications, J. Photochem. Photobiol. C Photochem. Rev. 15 (2013) 1–20. https://doi.org/10.1016/j.jphotochemrev.2012.10.001.

[77]   M.V. Dozzi, L. Prati, P. Canton, E. Selli, Effects of gold nanoparticles deposition on the

photocatalytic activity of titanium dioxide under visible light, Phys. Chem. Chem. Phys. 11 (2009) 7171–7180. https://doi.org/10.1039/b907317e.

[78] J. Wang, Y. Zhang, S. Wang, Y. Song, L. Jiang, Bioinspired colloidal photonic crystals with controllable wettability, Acc. Chem. Res. 44 (2011) 405–415. https://doi.org/10.1021/ar1001236.

[79] J. Wang, Y. Wen, J. Hu, Y. Song, L. Jiang, Fine control of the wettability transition temperature of colloidal-crystal films: From superhydrophilic to superhydrophobic, Adv. Funct. Mater. 17 (2007) 219–225. https://doi.org/10.1002/adfm.200600101.

[80] Q. Li, Z. Guo, Lubricant-infused slippery surfaces: Facile fabrication, unique liquid repellence and antireflective properties, J. Colloid Interface Sci. 536 (2019) 507–515. https://doi.org/10.1016/j.jcis.2018.10.083.

[81] M. Miyauchi, A. Nakajima, T. Watanabe, K. Hashimoto, Photoinduced hydrophilic conversion of TiO2/WO3 layered thin films, Chem. Mater. (2002). https://doi.org/10.1021/cm020355c.

[82] A. Srinivasan, M. Miyauchi, Chemically stable WO 3 based thin-film for visible-light induced oxidation and superhydrophilicity, J. Phys. Chem. C. (2012). https://doi.org/10.1021/jp303472p.

[83] M. Miyauchi, A. Nakajima, T. Watanabe, K. Hashimoto, Photocatalysis and photoinduced hydrophilicity of various metal oxide thin films, Chem. Mater. (2002). https://doi.org/10.1021/cm020076p.

[84] M. Miyauchi, Visible light induced super-hydrophilicity on single crystalline TiO2 nanoparticles and WO3 layered thin films, J. Mater. Chem. (2008). https://doi.org/10.1039/b718258a.

[85] T. Sarkar, S. Ghosh, M. Annamalai, A. Patra, K. Stoerzinger, Y.L. Lee, S. Prakash, M.R. Motapothula, Y. Shao-Horn, L. Giordano, T. Venkatesan, The effect of oxygen vacancies on water wettability of transition metal based SrTiO3 and rare-earth based Lu2O3, RSC Adv. (2016). https://doi.org/10.1039/c6ra22391e.

[86] S. Khan, G. Azimi, B. Yildiz, K.K. Varanasi, Role of surface oxygen-to-metal ratio on the wettability of rare-earth oxides, Appl. Phys. Lett. (2015). https://doi.org/10.1063/1.4907756.

[87] C. Mrabet, N. Mahdhi, A. Boukhachem, M. Amlouk, T. Manoubi, Effects of surface oxygen vacancies content on wettability of zinc oxide nanorods doped with lanthanum, J. Alloys Compd. (2016). https://doi.org/10.1016/j.jallcom.2016.06.286.

[88] S. Kim, H. Park, Sunlight-harnessing and storing heterojunction TiO2/Al 2O3/WO3 electrodes for night-time applications, RSC Adv. 3 (2013) 17551–17558. https://doi.org/10.1039/c3ra42644k.

[89] C.Q. Li, S.S. Yi, D.L. Chen, Y. Liu, Y.J. Li, S.Y. Lu, X.Z. Yue, Z.Y. Liu, Oxygen vacancy engineered SrTiO3 nanofibers for enhanced photocatalytic H2 production, J. Mater. Chem. A. (2019). https://doi.org/10.1039/c9ta03701b.

[90]   Q. Kang, J. Cao, Y. Zhang, L. Liu, H. Xu, J. Ye, Reduced TiO2 nanotube arrays for photoelectrochemical water splitting, J. Mater. Chem. A. (2013). https://doi.org/10.1039/c3ta10689f.

[91]   J. Bisquert, F. Fabregat-Santiago, I. Mora-Seró, G. Garcia-Belmonte, S. Giménez, Electron lifetime in dye-sensitized solar cells: Theory and interpretation of measurements, J. Phys. Chem. C. (2009). https://doi.org/10.1021/jp9037649.